

Far-infrared to centimeter emission of very nearby galaxies with archival data

L. Correia^{1,*}, C. Bot¹, J. Chastenet², A. Rymar¹, R. Paladini³, M. Bethermin¹, D. Ismail¹,
K. A. Lutz⁴, J.-P. Bernard⁵, A. Hughes⁵, D. Paradis⁵, and N. Ysard⁵

¹ Université de Strasbourg, CNRS, Observatoire astronomique de Strasbourg, UMR 7550, 67000 Strasbourg, France

² Sterrenkundig Observatorium, Ghent University, Krijgslaan 281-S9, 9000 Gent, Belgium

³ IPAC, California Institute of Technology, Pasadena, CA 91125, USA

⁴ DLR Galileo Competence Center, Oberpfaffenhofen, 82234 Wessling, Germany

⁵ Institut de Recherche en Astrophysique et Planétologie, Toulouse, France

Received 11 September 2025 / Accepted 20 November 2025

ABSTRACT

Compared to the well-studied infrared and radio domains, galaxy emission in the range from a few millimeters (mm) to centimeters (cm) (300–30 GHz) has been observed less frequently. In this domain, galaxy emission consists of thermal dust emission that is superimposed on free-free and synchrotron emission, with a possible additional contribution from anomalous microwave emission (AME) that peaks near 1 cm. We accurately characterize the integrated spectral energy distribution (SED) of galaxies in the mm–cm range. We used COBE-DIRBE, IRAS, *Planck*, and WMAP all-sky surveys brought to the same spatial resolution of $\sim 1^\circ$ to cover 18 photometric bands from 97 μm to 1.3 cm. Because of the low angular resolution and mixing with foreground and background emission that hampers the detection of the galaxy, our sample consists of six of the brightest nearby galaxies: the Large and Small Magellanic Clouds (LMC and SMC), M31, M33, NGC 253, and NGC 4945. We subtracted Milky Way dust emission, distant unresolved galaxies, and foreground point sources in the field. We fit each integrated SED with a model of thermal dust, free-free, synchrotron, AME, and cosmic microwave background (CMB) temperature fluctuations. The integrated SEDs of our sample of galaxies are well fit by the model within the uncertainties, although degeneracies between the different components contributing to the mm–cm emission complicate the estimation of their individual contributions. We did not clearly detect AME in any of our target galaxies, and the AME emissivity upper limits are weak compared to Galactic standards. This suggests that the AME signal might be diluted at the scale of a whole galaxy. We inferred positive CMB fluctuations in the background of five out of our six galaxies. This effect might be related to the degeneracy between the dust emissivity index and CMB fluctuations in the background, or it might be linked to the specific spatial distribution of CMB fluctuations coupled with our 1° resolution and small number statistics.

Key words. ISM: general – galaxies: ISM – Local Group – Magellanic Clouds – submillimeter: ISM

1. Introduction

The emission of a galaxy is dominated by stellar light in the ultraviolet to near-infrared, by dust emission in the mid- and far-infrared (FIR), and by free-free and synchrotron emission in the radio domain. Synchrotron and free-free emission are typically represented as the superposition of two power-law spectra. Dust emission in the far-infrared is the thermal emission of large dust grains at thermal equilibrium with the radiation field, and it is often represented as a modified blackbody spectrum or as the sum of modified blackbodies.

Simple dust emission laws have been challenged by observations in the past decades. In particular, observations in the infrared (IR) to submillimeter (submm) range have shown breaks or a flattening in the dust emissivity law at long wavelengths in galaxies, which was described on occasion as a submm excess above a given fixed emissivity power-law index dust model (e.g., Lisenfeld et al. 2002; Bendo et al. 2006; Gordon et al. 2014). Changes in the submm emissivity might be linked to changes in optical properties of dust grains with environmental conditions (e.g., Demyk et al. 2022). Based on these laboratory measurements, Ysard et al. (2024) have demonstrated that the

corresponding variations in the intrinsic optical properties of the grains are sufficient to reproduce the range of emissivity spectral index values observed in the diffuse interstellar medium of the Milky Way. These changes might also simply be interpreted as revealing the cold dust of galaxies (e.g., Rémy-Ruyer et al. 2013). A particularly flat dust emissivity was shown to extend to mm wavelengths (e.g., Hermelo et al. 2013; Tibbs et al. 2018). This effect was observed in the Large and Small Magellanic Clouds (LMC and SMC) up to the cm range (Israel et al. 2010; Bot et al. 2010; Planck Collaboration XVII 2011), which excludes cold dust as a possible origin. Positive fluctuations in the temperature of the cosmic microwave background (CMB) can explain the cm excess in the LMC, but they do not explain this fully in the SMC. It is still unclear which emission process produces this long-wavelength emission excess above classical dust models, but possibilities include magnetic dipole emission from magnetic nanoparticles (Draine & Hensley 2012), specific emission properties of amorphous solids (Meny et al. 2007), or spinning dust emission (Bot et al. 2010).

The CMB fluctuations can be a significant background emission component comparable to the emission of these galaxies, primarily because the SMC and LMC have a low surface brightness. The metallicity of these galaxies is lower than the reference

* Corresponding author: lucie.correia@astro.unistra.fr

values in the solar neighborhood, and they are dust poor (Clark et al. 2021; Roman-Duval et al. 2022; Clark et al. 2023). Furthermore, the thermal dust Rayleigh-Jeans tail is exponentially fainter at long wavelengths, and because the angular sizes of the SMC and LMC are several degrees on the sky, this emission is spread across large areas. As a consequence, the mm-to-cm ($\sim 300\text{--}30$ GHz) dust brightness of these galaxies is comparable to the emission of CMB fluctuations. Studies of M31 or M33 have also shown the effect of CMB fluctuations on the observed spectral energy distribution (SED) (Planck Collaboration Int. XXV 2015; Tibbs et al. 2018; Harper et al. 2023). While they do not dominate the mm–cm emission of the galaxy, CMB fluctuations in the background have to be taken into account when the emission of the galaxy itself is studied. It is an open question whether dust emission with a flat emissivity index might erroneously be interpreted as part of the background CMB fluctuations. This possibility is supported by the fact that previous mm-to-cm SED studies of the SMC, LMC, and M31 all required a positive CMB fluctuation in the background of these galaxies. Furthermore, some recent studies have suggested that an unmodeled emission component associated with galaxies might bias current CMB fluctuation maps (Luparello et al. 2022; Hansen et al. 2023; Lambas et al. 2024).

In addition to thermal dust, free-free, and synchrotron emissions in the mm–cm range, a specific component of the dust emission is the anomalous microwave emission (AME, Dickinson et al. 2018). The AME peaks around 1 cm (30 GHz), and has been known for several decades (e.g., Kogut et al. 1996; Leitch et al. 1997). Extensively observed and studied in our own galaxy (e.g., Watson et al. 2005; Planck Collaboration XV 2014; Poidevin et al. 2018; Cepeda-Arroita et al. 2021; Fernández-Torreiro et al. 2023b), the currently favored emission mechanism is electric dipole radiation from small spinning dust grains in the ISM (Draine & Lazarian 1998a,b; Ali-Haïmoud et al. 2009; Bell et al. 2019; Casassus et al. 2021; Ysard et al. 2022). Extragalactic detections of AME remain rare, and when reported, were confined to localized regions within galaxies, such as a star-forming region in NGC 6946 (Murphy et al. 2010; Hensley et al. 2015) and a compact radio source associated with NGC 7425 (Murphy et al. 2018, 2020). Additional extragalactic detections are essential for constraining the variation in AME in different galactic environments. Poojon et al. (2024) detected AME in NGC 2903 and marginally in NGC 2146, with higher-frequency, stronger spinning dust emission that was consistent with predictions for denser environments such as molecular clouds and PDRs. The only detection of AME in the integrated emission of a galaxy so far is in M31 (Planck Collaboration Int. XXV 2015; Battistelli et al. 2019), although the significance of the detection varied depending on the data that were used (Poidevin et al. 2018; Harper et al. 2023). The presence of AME was also studied in the integrated emission of the galaxies M82, NGC 253, and NGC 4945 by Peel et al. (2011), M33 by Tibbs et al. (2018), NGC 3627, NGC 4254, NGC 4736, and NGC 5055 by Bianchi et al. (2022), but only upper limits were established. It was found that the integrated emission was lower than expected, based on the ratio of FIR to AME in the Galaxy.

While the IR to submm emission of galaxies has been extensively studied, their mm-to-cm emission remains poorly constrained. Ground-based observations of nearby galaxies in this wavelength range have a good spatial resolution, but require large-scale filtering (e.g., Smith et al. 2021), long observations, and precise processing to detect emission beyond the brightest regions of the galaxy given the current instrument and antenna

Table 1. Celestial coordinates and distances for the sample of galaxies.

Galaxy	α (J2000)	δ (J2000)	d (Mpc)
SMC	00 ^h 52 ^m 38 ^s	−72°48′01″	0.06
LMC	05 ^h 23 ^m 35 ^s	−69°45′22″	0.049
M31	00 ^h 42 ^m 44 ^s	+41°16′07″	0.785
M33	01 ^h 33 ^m 51 ^s	+30°39′36″	0.809
NGC 253	00 ^h 47 ^m 33 ^s	−25°17′20″	3.215
NGC 4945	13 ^h 05 ^m 27 ^s	−49°28′04″	4.61

Notes. Distances are taken from Muñoz et al. (2018); Richter et al. (1987); McConnachie et al. (2005); Springob et al. (2005); Allison et al. (2014).

sensitivities (e.g., IMEGIN large program with IRAM 30m led by S. Madden, Katsioli et al. 2023; Ejlali et al. 2025). It is unclear, however, how much dust exists in the diffuse outer parts of galaxies, and this might be significant. For example, Ménard et al. (2010) suggested that half of the dust in galaxies might lie in extended halos. In this context, all-sky surveys made with satellite missions such as COBE-DIRBE, IRAS, *Planck*, and WMAP hold the potential to detect every sufficiently bright galaxy and capture their integrated IR-to-microwave emission. However, their low angular resolution leads to mixing with foreground and background emission (including Galactic cirrus, extragalactic sources, and CMB fluctuations), which must be separated and removed.

We characterized the integrated SED of a sample of nearby galaxies in the mm to cm range. For this, we used COBE-DIRBE, IRAS, *Planck*, and WMAP archival all-sky surveys, convolved to the same $\sim 1^\circ$ resolution and without cirrus emission and point sources, to obtain the emission of our target galaxies from 97 μm to 13 mm in 18 photometric bands. We complemented these SEDs with archival radio flux densities from the literature and modeled the resulting SEDs with a simple model of thermal dust emission, free-free, AME, and synchrotron for the galaxy, and with CMB fluctuations in the background. In principle, any galaxy or point source that is detected in all bands could be studied, but these detections are hard for nearby galaxies because the resolution is limited and the foreground–background subtraction has large uncertainties. We focused on six bright, nearby galaxies that are listed in Table 1. These galaxies were previously studied with *Planck*, but the results are difficult to compare because the methods and datasets that were employed differ. We excluded M82 from our sample because it is strongly contaminated by the Milky Way foreground at the common resolution of $\sim 1^\circ$. M31, M33, and the LMC and SMC are part of the Local Group, while NGC 253 and NGC 4945 are more distant. NGC 253 and NGC 4945 are both highly active spiral galaxies that are characterized by intense starburst star formation in their central region. NGC 4945 also hosts an obscured Seyfert 2-type active nucleus.

The paper is organized as follows. Section 2 presents the data we used in our analysis. Section 3 describes the processing we used to obtain the galaxy maps for the study, including the foreground and background subtraction. In Section 4 we describe our model of dust, free-free, synchrotron, and AME emission for the studied galaxy and CMB fluctuations in the background. The results are presented in Section 5 and discussed in Section 6. Finally, our conclusions are presented in Section 7.

2. Data

We used archival data from all-sky surveys to cover the emission from the IR peak to cm wavelengths, complemented by radio flux densities that we compiled from the literature.

2.1. IRAS

The Infrared Astronomical Satellite (IRAS; Neugebauer 1984), launched in 1983, mapped the full sky at 12, 25, 60, and 100 μm . For this study, we used the 100 μm IRIS maps from Miville-Deschênes & Lagache (2005) to benefit from improved zodiacal light subtraction, calibration, and zero-level accuracy, allowing us to model the peak of thermal dust emission. We adopted a calibration uncertainty of 13.5% and a beam width of $\approx 4'$ (Hauser et al. 1998; Miville-Deschênes & Lagache 2005).

2.2. COBE-DIRBE

The Cosmic Background Explorer (COBE; Mather et al. 1990), launched in 1989, mapped the sky with three instruments from 1.2 to 240 μm . We used three bands of DIRBE¹ at 100, 140, and 240 μm to further constrain the peak of the thermal dust spectrum, and with zodiacal light already subtracted. The uncertainties in the gain calibration for these bands are 13.5, 10.6, and 11.6 % for the bands at 100, 140, and 240 μm , respectively (Hauser et al. 1998). Although the DIRBE beam is significantly non-Gaussian, as shown by Cambrésy et al. (2001), due to multiple scan directions, the data products we used can be approximated by a rotation-averaged Gaussian beam with a width of 1° .

2.3. WMAP

The Wilkinson Microwave Anisotropy Probe (WMAP), launched in 2001, mapped the sky in five bands: 3.2, 4.9, 7.3, 9.1, and 13 mm (93.5, 60.7, 40.7, 33.0, and 22.8 GHz respectively) at a resolution between $12.6'$ for the lower wavelength and $55.8'$ for the higher wavelength. We used final nine-years data delivery maps¹ (DR5; Bennett et al. 2013). As the instrumental noise is not a limiting factor, we assumed a 3% overall calibration uncertainty, as used in other studies (Planck Collaboration XV 2014).

2.4. Planck

The *Planck* satellite, launched in 2009, observed the sky with two instruments, the High Frequency Instrument (HFI; Planck Collaboration VII 2014), covering the bands at 350, 500, 850 μm , and 1.3, 2.1, 3 mm (857, 545, 353, 217, 143, 100 GHz, respectively) and the Low Frequency Instrument (LFI; Planck Collaboration XII 2014) covering three bands centered at 4.3, 6.8, and 10 mm (70, 44, and 30 GHz respectively). The angular resolution is between $5'$ at the highest frequency and $30'$ for the lowest (Planck Collaboration I 2011). We adopted calibration uncertainties of 7% for HFI bands (Planck Collaboration VII 2014) and 3% for LFI bands (Planck Collaboration XII 2014). We used data from the last release “*Planck* Public Release 4” published in 2020.

We also used some of the *Planck* data products obtained from component separations and downloaded from *Planck* Legacy Archive²: COMMANDER CMB fluctuation maps

(Planck Collaboration IV 2020), CIB (Planck Collaboration Int. XLVIII 2016) and CO maps (Planck Collaboration XIII 2014). These maps were used to characterize the foreground dust emission associated with molecular clouds, to account for background emission from distant unresolved galaxies, and to remove a first CMB fluctuation estimate around our galaxies to determine the background zero level emission (see Section 3.2).

2.5. Radio data

For each galaxy studied, we gathered radio flux densities from the literature by using the NASA/IPAC Extragalactic Database³ (NED) and VizieR SED photometry services⁴. We prioritized flux densities obtained with single-dish radio telescopes over those from interferometric observations. This choice was motivated by the idea that single-dish measurements are more sensitive to diffuse and extended emissions while interferometric data might resolve them out. We focused exclusively on data in the radio domain down to 0.3 GHz, which reflects both the limited availability of high-resolution data at lower frequencies and the known turnover of the synchrotron spectrum below ~ 1 GHz, where a simple power-law approximation becomes unreliable. Restricting the analysis to this frequency range ensures robust constraints on synchrotron and free-free emission models. The radio data we used are listed in the appendix for each galaxy (from Tables A.1 to A.6).

2.6. Literature IR-mm data

For consistency and comparison, we added IR–mm data from the literature, including both similar resolution and higher-resolution observations (e.g., from *Herschel*, IRAM 30 m). These data are not used in our modeling, but we used them for comparison to our fiducial measurements, and to check whether there is evidence for extended emission in the integrated SEDs.

2.7. Ancillary data

In order to assess the contribution of foreground emission from dust in the Milky Way, we use gas maps as templates. For the atomic hydrogen gas, we used the HI 4-PI Survey (HI4PI) (HI4PI Collaboration 2016), built from the Effelsberg-Bonn HI Survey at a resolution of $16.2'$. Because we are interested in using these maps for the Milky Way foreground only, we took the integrated HI column density maps corresponding to velocities between -90 and 90 km/s.

To trace the ionized gas, we used the Finkbeiner (2003) full-sky $\text{H}\alpha$ map, which combines reprocessed Virginia Tech Spectral line Survey (VTSS), Southern H-Alpha Sky Survey Atlas (SHASSA), and Wisconsin H-Alpha Mapper (WHAM) Northern Sky Survey data. VTSS and SHASSA were calibrated to the WHAM zero point and reprocessed to remove artifacts, producing a well-sampled map at $6'$ FWHM.

3. Data processing

3.1. Combination of all-sky surveys

The combination of IRAS, DIRBE, *Planck*, and WMAP maps allows us to explore nearby galaxy emission in 18 photometric bands, from the peak of thermal dust emission in the FIR up

¹ <https://lambda.gsfc.nasa.gov/>

² <https://pla.esac.esa.int/>

³ <https://ned.ipac.caltech.edu/>

⁴ <https://vizier.cds.unistra.fr/>

to cm wavelength, a wide frequency coverage. These data are encoded in the HEALPix format (Hierarchical Equal Area isoLatitude Pixelisation; Górski et al. 2005). To allow direct pixel-to-pixel comparison, all maps were smoothed to a common resolution of 1° using the smooth function of the healpy package, applying a Gaussian approximation. This resolution corresponds to the lowest of our sample, defined by the 13 mm band of WMAP and the DIRBE data. Given the low angular resolution, the sampling was reduced to a consistent HEALPix grid of $N_{\text{side}} = 256$ (pixel angular size of $\sim 13.7'$). All maps were converted into the same unit, MJy/sr, using conversion factors from K_{cmb} to MJy/sr listed in Lagache et al. (2020) for *Planck* and in the Planck Sky Model⁵ for WMAP.

3.2. Subtracting foreground and background emissions

At the low angular resolution of this study (1°), foreground and background emission superimpose and mix together with the emission of the galaxy we want to study: zodiacal light, Milky Way dust emission, other point sources close in projection to the galaxy, unresolved galaxies in the background and CMB fluctuations all emit at IR to radio wavelengths. While some of these emission components like zodiacal light are sufficiently large scale or faint to be ignored, the other ones can be significant or even brighter than the emission of the galaxy itself. We attempted to remove these emissions using template maps, except for CMB fluctuations that we model together with the studied galaxies. Here we briefly describe the overall process for foreground and background subtraction.

3.2.1. CMB fluctuations

At mm-to-cm wavelengths, CMB fluctuations contribute significantly and may even dominate the total observed signal in the mm–cm regime. Different CMB temperature fluctuation maps based on different component separation methods exist (Planck Collaboration IV 2020; Planck Collaboration LVII 2020). Previous analyses of nearby galaxies (e.g., Tibbs et al. 2018; Harper et al. 2023) have shown that the choice of the component separation map that is used for CMB temperature fluctuations can change the resulting physical parameters estimated for the galaxy. Furthermore, these CMB fluctuation maps cannot always be trusted in the direction of our studied galaxies and are imprinted or masked in the maps that are openly available. This is due to the fact that CMB fluctuation signal can be partially degenerate with dust and radio emission, complicating their removal (e.g., Planck Collaboration XVII 2011; Bobin et al. 2016). In this paper, we modeled CMB fluctuations jointly with the galaxy emission components. We used the COMMANDER CMB maps (Planck Collaboration LVII 2020) for visualizing the CMB fluctuations, and for estimating a CMB-free background level around each galaxy, but CMB fluctuations are not removed from the integrated SEDs that we analyzed. We adopted the COMMANDER PR4 products for consistency with the PR4 intensity maps and because they perform best in regions strongly contaminated by Galactic dust and other foregrounds (Planck Collaboration LVII 2020).

3.2.2. Removing foreground and background sources

Other galaxies and compact sources in our fields can bias our background estimates, foreground subtraction, and create additional scatter in the dust–gas correlation that we use to

remove extended foreground dust emission. To address this, we subtracted all resolved sources located within the fields of our targets using the source catalogs of each all-sky survey: the COBE/DIRBE Point Source Catalog (Smith et al. 2004), the IRAS Galaxies+QSOs Catalog (Fullmer & Lonsdale 1995), the *Planck* PCCS2 and PCCS2E (Planck Collaboration XXVI 2016), and the WMAP Nine-Year Source Catalog (Bennett et al. 2013).

In the case of M31, a source located close to the galaxy affects the measured fluxes and, consequently, the shape of its integrated SED. The analysis by Harper et al. (2023) is more accurate in this respect, as they rely on higher-resolution studies to correct for this effect. In our work, we aimed to apply a consistent methodology across all galaxies, and we do not have comparable high-resolution data for the entire sample. We therefore adopted a uniform approach for all galaxies, that does not specifically correct for this source.

For each photometric band, we generated a source map on a Healpix grid at the survey resolution by projecting catalog fluxes at the listed positions and converting them to MJy/sr. Catalogs often provide multiple flux estimates depending on the extraction method. For *Planck*, GAUFLUX is adopted for extended sources and DETFLUX for compact ones. We considered sources as extended if the geometric mean of the fit ellipse exceeds 1.5 times the beam FWHM (Planck Collaboration XXVI 2016). We took care to avoid subtracting emission intrinsic to our target galaxies. Specifically, we excluded all catalog sources within 2° of the SMC and M31, 5° of the LMC, and 0.1° of M33, NGC 253, and NGC 4945. This ensures that the entire emission of these galaxies, which may be divided into several sub-sources in some catalogs, is not inadvertently subtracted.

The resulting source maps were smoothed to 1° , degraded to $N_{\text{side}} = 256$, and subtracted from the intensity map for each photometric band.

3.2.3. Zero-level estimation and CIB removal

The cosmic infrared background (CIB) arises from the integrated emission of unresolved extragalactic sources, including distant galaxies and quasars. Although it contributes to the overall FIR intensity maps, its effect is minimized in our analysis through local background subtraction around each region of interest. Consequently, the absolute zero level of the maps does not influence our results.

In addition to a constant background, CIB emission has also anisotropies, reflecting both the large-scale clustering of the contributing sources and their intrinsic luminosity variations (Planck Collaboration XVIII 2011). To estimate the spatial distribution of the CIB, we inspected the CIB *Planck* maps at 350, 500, and 850 μm in MJy/sr (Planck Collaboration XVIII 2011), but we did not find these fluctuations to be significant for our study.

3.2.4. CO line contribution to the photometric bands

Planck maps at 1.3 and 3 mm (217 and 100 GHz) can contain significant $J = 2 \rightarrow 1$ or $J = 1 \rightarrow 0$ CO line emission (Planck Collaboration XIII 2014) on top of the dust emission, from foreground Milky Way interstellar gas or from the molecular gas of the galaxy we study. Although these contributions can be estimated from *Planck* CO maps (Planck Collaboration XIII 2014), we chose to omit the 1.3 and 3 mm bands from the SED fitting to avoid bias.

3.2.5. Foreground of the Milky Way dust emission

Dust in the Milky Way is emitting in every region of the sky, even at high Galactic latitude where our galaxies are located. We

⁵ Planck Sky Model User Manual: https://apc.u-paris.fr/~delabrou/PSM/Public/PSM_user_manual_v1.7_8.pdf

therefore need to remove this dust emission in the foreground of the galaxies we want to study. The foreground emission is more prominent in the FIR but extends to all wavelength bands (Planck Collaboration XVII 2014). Because gas and dust are correlated, we can use gas tracers to estimate the dust emission foreground and subtract it to the all-sky surveys we use. In Section 3.2.3, we already used this correlation at high Galactic latitude to define a first order background emission for the sky. Here, we want to use gas maps as templates for the dust emission in the foreground. The idea is to estimate dust–gas emissivity factors, apply these to the gas map to compute a template of foreground dust emission in each band, and remove it in front of our studied galaxies.

Although Planck Collaboration XVII (2014) estimated well-constrained dust-to-HI ratios for the diffuse and high-latitude sky, variations of these ratios around their average values exist on the sky (Bot et al. 2009; Planck Collaboration XXIV 2011; Planck Collaboration XVII 2014) and correspond to actual variations of dust properties (Ysard et al. 2024). In order to take into account these variations in the dust emissivity and temperatures of the foreground, we chose to perform a local estimate of the cirrus foreground around each galaxy. Further details are provided in Appendix B.

3.2.6. Resulting foreground- and background-subtracted maps

Figures 1a and 1b show the maps of M31 as an example before and after subtraction of the CMB fluctuations, CIB, individual sources and dust in the foreground as presented in this section. Comparing with Figure 1a, we can see that the galaxy in Figure 1b is therefore well detected, even at long wavelengths. At 3.2 and 4.9 mm, the data are significantly noisier, limiting the signal quality in these bands. The maps after the subtraction of the foreground and background emissions for the other galaxies of the sample are presented on the public platform [Zenodo](#).

3.3. Projection and aperture photometry

After subtraction of the different foreground and background emissions for each galaxy of our sample, we projected all maps on a 30×30 pixel grid centered on each galaxy and with a pixel size of $13.74'$. The LMC and SMC being extended galaxies (respectively 8° and 2°), we built pixel grids of 100×100 pixels for LMC and 50×50 pixels for SMC. The galaxy coordinates (and hence central pixels) were taken from the SIMBAD database⁶ and are summarized in Table 1. The maps we obtained and used for each galaxy before and after subtraction are presented for all 18 bands in Figures 1a and 1b for M31 as an example, and on [Zenodo](#) for the other galaxies of our sample.

To obtain the integrated flux density of each galaxy, we performed aperture photometry on the galaxy maps in all bands. The emission at the galaxy’s position is determined by measuring the flux density within a region centered on the galaxy (“ON” region) and subtracting the background emission estimated in an annulus surrounding the galaxy (“OFF” region). For the SMC, LMC and M31, we chose the same apertures as in Planck Collaboration XV (2014) and Planck Collaboration Int. XXV (2015). For M33, NGC 253 and NGC 4945, we took a circular region with a radius of $80'$ surrounded by an annulus of radius

$42'$ that is offset further out. The ON and OFF regions we used are delineated by the solid and dashed white lines, respectively. We emphasize that we have chosen to measure the integrated flux density of the galaxy in the central region, on the convolved and foreground/background subtracted maps, except for the CMB fluctuations that are kept in and will be taken into account in the modeling. For the background (OFF) region, we took the median of the surface brightnesses on the convolved maps with all foreground and background emissions removed (including the CMB fluctuations), to ensure that the average background level is not mainly driven by the CMB temperature fluctuations.

Most of the uncertainty on the integrated fluxes of the galaxies comes from remaining variations due to the imperfect foreground and background emission subtractions. We quantified this source of uncertainty by computing the standard deviation of the surface brightnesses observed in the background region around each galaxy, as measured in maps with all foreground and background emission subtracted (including the CMB fluctuations). We then added these uncertainties quadratically to the calibration gain uncertainties from the instruments.

The resulting flux densities in all 18 bands from $\sim 100 \mu\text{m}$ to 1.3 cm for each galaxy are listed in Table 2 and plotted as a function of frequency with gray points in Figures 2, 4, 5, and 6. These obtained integrated SEDs are complemented with the radio data from the literature as described in Section 2.5 and listed in Appendix A. These flux densities constitute a complete set of integrated SEDs from the IR to the radio domain, with excellent mm–cm coverage. They include both the galaxy emission and background CMB fluctuations, which we modeled jointly and analyzed in the following sections.

4. Emission model

Since we expected the galaxy emission in the mm-to-cm range to be a combination of dust, free-free, synchrotron and AME, with the presence of CMB fluctuations in the background, and each of these components have a specific spectral shape, we used a model that is a combination of these different contributions, following the approach of Harper et al. (2023).

The integrated emission of the galaxy was modeled as:

$$S_{\text{tot}}(\nu) = S_{\text{dust}} + S_{\text{AME}} + S_{\text{ff}} + S_{\text{syn}} + S_{\text{CMB}}, \quad (1)$$

where $S(\nu)$ are flux densities in Jy at a given frequency band.

4.1. Dust emission

Dust emission dominates the FIR–mm regime of galaxies and can be modeled in various ways: from full dust models (e.g., Draine & Li 2001; Jones et al. 2013; Köhler et al. 2014, 2015; Ysard et al. 2015; Siebenmorgen 2023; Hensley & Draine 2023; Ysard et al. 2024) and mixing recipes accounting for environmental and heating variations (e.g., Dale et al. 2001; Dale & Helou 2002; Draine & Li 2007; Galliano 2018), to more phenomenological approaches (e.g., Gordon et al. 2014; Chiang et al. 2018). Here we adopted a simple modified blackbody since (1) the FIR–mm emission is dominated by large grains in thermal equilibrium, (2) we aim to limit the number of free parameters in our multicomponent model, (3) the integrated SEDs of nearby galaxies are well described at long wavelengths by this model (e.g., Harper et al. 2023), and (4) it facilitates comparison with other studies, including at higher redshift (e.g., Ismail et al. 2023).

⁶ <https://simbad.cds.unistra.fr/simbad/>

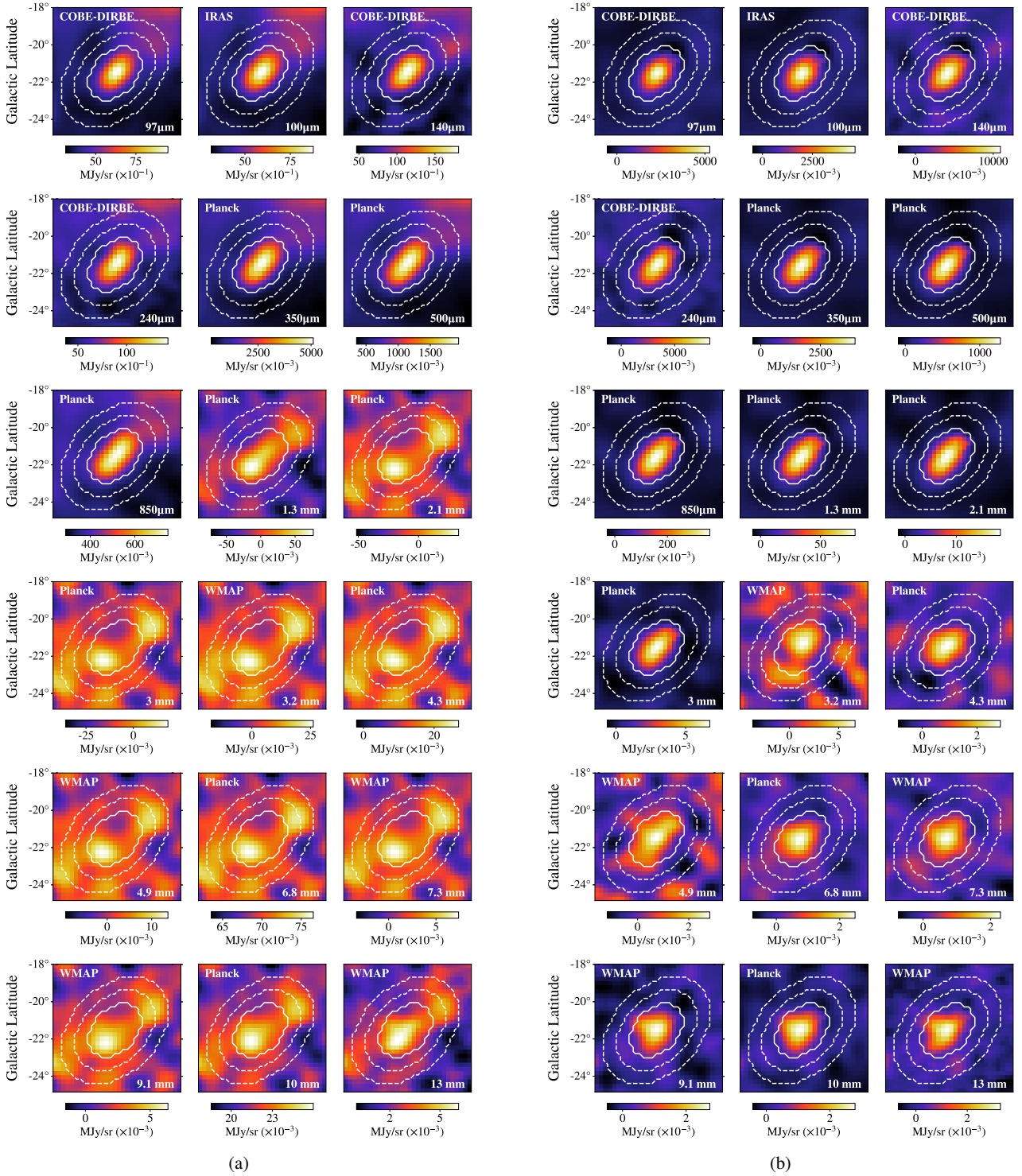


Fig. 1. (a) Maps of M31 at a resolution of 1° , in 18 photometric bands of COBE-DIRBE, IRAS, *Planck* and WMAP from $97 \mu\text{m}$ to 1.3 cm , before the foreground and background emissions were subtracted. (b) Maps around M31 after the foreground and background sources subtraction. The solid and dashed white lines delineate the on-source and background regions we used for the aperture photometry, respectively.

Our simple dust emission model is hence described as a single modified blackbody as

$$S_{\text{dust}} = \frac{2h\nu^3}{c^2} \left(\frac{\nu}{353 \text{ GHz}} \right)^\beta \tau_{353} \left(e^{h\nu/k_b T_d} - 1 \right)^{-1} \Omega, \quad (2)$$

with the free parameters β the dust emissivity index, τ_{353} the optical depth at 353 GHz, and T_d the dust temperature (in K). ν

is the observed frequency in GHz, and Ω is the solid angle of the aperture (in sr).

4.2. Anomalous microwave emission

The spinning dust component was modeled as

$$S_{\text{AME}}(\nu) = C_{\text{AME}} S_{\text{spin}}(\nu) \Omega, \quad (3)$$

Table 2. Integrated flux densities (in Jy) obtained for each galaxy from the foreground- and background-subtracted maps with CMB fluctuations.

Mission	λ (μm)	ν (GHz)	LMC	SMC	M31	M33	NGC 253	NGC 4945
COBE	97	3000	156 000 \pm 44 000	13 400 \pm 3800	2290 \pm 652	972 \pm 276	2050 \pm 583	1783 \pm 506
IRAS	100	3000	182 000 \pm 25 600	14 000 \pm 2420	2730 \pm 474	990 \pm 284	1690 \pm 270	1770 \pm 946
COBE	140	2141	190 000 \pm 51 500	13 100 \pm 3550	5006 \pm 1360	1287 \pm 349	2190 \pm 595	2108 \pm 572
COBE	240	1250	112 000 \pm 31 000	8390 \pm 2310	3927 \pm 1080	1260 \pm 347	969 \pm 267	1520 \pm 419
Planck	350	857	71 900 \pm 8470	6300 \pm 1360	2679 \pm 237	636 \pm 146	481 \pm 65	850 \pm 618
Planck	500	545	24 600 \pm 3100	2570 \pm 463	920 \pm 85	239 \pm 51	132 \pm 21	248 \pm 210
Planck	850	353	7554 \pm 842	899 \pm 130	281 \pm 20	80 \pm 14	35 \pm 5	49 \pm 61
Planck	1300	217	2208 \pm 189	266 \pm 30	83 \pm 5	25 \pm 4	11 \pm 1	-12 \pm 14
Planck	2100	143	848 \pm 51	99 \pm 7	29 \pm 1	9.6 \pm 0.9	5.2 \pm 0.4	-18 \pm 4
Planck	3000	100	479 \pm 21	52 \pm 3	16 \pm 1	5.2 \pm 0.5	3.3 \pm 0.4	-12 \pm 1
WMAP	3200	93.5	417 \pm 24	43 \pm 6	13 \pm 2	3.7 \pm 1.7	3.6 \pm 2.4	-13 \pm 2
Planck	4300	70	283 \pm 11	29 \pm 2	7.5 \pm 0.6	2.4 \pm 0.5	1.4 \pm 0.4	-5.7 \pm 0.7
WMAP	4900	60.7	244 \pm 12	23 \pm 3	6.8 \pm 0.8	3.0 \pm 0.9	1.8 \pm 0.8	-3.9 \pm 0.7
Planck	6800	44	191 \pm 9	18 \pm 2	3.9 \pm 0.4	1.1 \pm 0.4	1.4 \pm 0.2	-1.8 \pm 0.7
WMAP	7300	40.7	189 \pm 8	17 \pm 2	3.6 \pm 0.4	1.2 \pm 0.5	1.2 \pm 0.5	-1.3 \pm 0.9
WMAP	9100	33	176 \pm 8	15 \pm 2	3.3 \pm 0.3	1.0 \pm 0.4	1.2 \pm 0.4	-0.1 \pm 0.9
Planck	10 000	30	169 \pm 9	15 \pm 2	2.9 \pm 0.3	0.99 \pm 0.28	1.3 \pm 0.3	0.13 \pm 0.96
WMAP	13 000	22.8	173 \pm 9	14 \pm 2	2.7 \pm 0.4	0.82 \pm 0.42	1.4 \pm 0.4	0.69 \pm 1.21

where we took S_{spin} as the AME emission spectrum in MJy/sr for the diffuse Milky Way dust reference, and the free parameter C_{AME} acts as the scaling factor of AME. As stated in Ysard et al. (2022), spinning dust models using carbonaceous nano-grains give comparable results regardless of their exact nature, PAHs as in SpDust or amorphous hydrocarbons as in THEMIS⁷ (The Heterogeneous dust Evolution Model for Interstellar Solids, Jones et al. 2013, 2014; Köhler et al. 2014, 2015; Ysard et al. 2015), the model that we used. We modeled the spinning dust component as a fixed template representing the warm neutral medium as defined by Draine & Lazarian (1998b) and Weingartner & Draine (2001), with a fixed peak frequency at 31 GHz.

4.3. Free-free emission

Free-free emission, arising from electrons accelerated in the electric field of diffuse gas and ionized regions (Condon 1992), exhibits a nearly flat spectrum: at low frequencies its intensity rises roughly as ν^2 with an almost constant brightness temperature, whereas at high frequencies the intensity decreases slowly as $\nu^{-0.1}$. Consequently, significant degeneracies can arise between the free-free component and other emissions, particularly synchrotron and AME. We modeled free-free emission as

$$S_{\text{ff}} = \frac{2 k_b T_{\text{ff}} \Omega \nu^2}{c^2}, \quad (4)$$

where $T_{\text{ff}} = T_e (1 - e^{-\tau_{\text{ff}}})$ is the free-free brightness temperature, T_e is the electron temperature⁸, and τ_{ff} is the free-free optical depth. The optical depth is defined by Draine (2011)

$$\tau_{\text{ff}} = 5.468 \times 10^{-2} T_e^{-1.5} \nu_{\text{GHz}}^{-2} EM g_{\text{ff}}, \quad (5)$$

with the emission measure EM in pc cm⁻⁶, and the Gaunt factor g_{ff} derived from Draine (2011). In this free-free emission model, the only free parameter is EM.

⁷ <https://www.ias.u-psud.fr/themis/>

⁸ We assumed a fixed electron temperature of 8000 K (Planck Collaboration XV 2014) and singly ionized scattering ions.

4.4. Synchrotron emission

Synchrotron emission results from the acceleration of ultra-relativistic electrons within magnetic fields, and its spectral distribution is generally well represented by a power-law function (Condon 1992). Accordingly, we modeled the synchrotron emission with a simple power law,

$$S_{\text{syn}} = C_{\text{syn}} \nu^{\alpha_{\text{syn}}}, \quad (6)$$

with two free parameters: C_{syn} is the synchrotron amplitude at 1 GHz, and α_{syn} is the spectral index of the flux density.

4.5. Background CMB fluctuation emission

We took into account the CMB fluctuations in our model. Their flux densities were modeled as

$$S_{\text{CMB}}(\nu) = \frac{2 h \nu^4}{c^3 T_{\text{CMB}}} \frac{x e^x}{e^x - 1} \delta_{\text{CMB}} \Omega, \quad (7)$$

with $x = h\nu/k_b T_{\text{CMB}}$, T_{CMB} the temperature of the CMB (2.72548 K; Fixsen 2009), and the free parameter δ_{CMB} corresponding to the amplitude of CMB temperature fluctuations in K. Modeling the CMB fluctuations together with the galaxy emission allows us to explore possible degeneracies between free parameters.

4.6. Fitting with a Markov Chain Monte Carlo method

The SEDs we fit correspond to the emission integrated in a set of 18 photometric bands from the different instruments. For a fair comparison, we integrated our total model (equation 1) in the same photometric bands as well. We did this using the band-pass filters from each instrument and integration libraries from the DustEM IDL tool⁹ (Compiègne 2011). To fit our emission model (with eight free parameters; β , τ_{353} , T_d , C_{AME} , C_{ff} , C_{syn} , α_{syn} and δ_{CMB}) integrated into photometric bands, to the observed SED of each galaxy, we used a combination of two fitting methods.

⁹ <http://dustemwrap.irap.omp.eu/>

We began with a PYTHON NUMPY Levenberg–Marquardt (Levenberg 1944; Marquardt 1963) nonlinear least-squares method to minimize the difference between our model and the observed SED. We provided initial guesses for the model parameters ($\beta \in [0, 3]$, $\log_{10} \tau_{353} \in [-8, 8]$, $T_d \in [10, 50]$ K, $C_{\text{ff}} \in [0, 10]$, $C_{\text{syn}} \in [0, 100]$, $\alpha_{\text{syn}} \in [-5, 5]$, $\delta_{\text{CMB}} \in [-50, 50]$ μK , and $C_{\text{AME}} \in [0, 5]$)¹⁰, and we assumed additive Gaussian noise with independent errors for each photometric band, using the reported observational uncertainties to weight the fit. This method provides a first estimate of the best-fit parameters and their associated uncertainties, obtained as the square root of the diagonal elements.

We then used the emcee (Foreman-Mackey et al. 2019) implementation to do a Markov Chain Monte Carlo (MCMC) fitting. This second step allows us to better explore the parameter space and study the potential degeneracies between model parameters. The MCMC process is initialized with the start parameters found by the least-squares fitting. Uniform priors were applied to all parameters, with positivity enforced for all amplitude parameters except the CMB anisotropy. For this work we used 200 chains, that run for 10 000 iterations, with a burn-in of 4000 samples to allow the chains to converge. Finally, we thin the chains by taking every 15th sample to remove sample-to-sample correlations, ensuring the final samples are independent for a robust parameter estimation.

While the Levenberg–Marquardt step provides a quick and approximate best-fit solution, the MCMC step gives the full posterior probability distribution for each parameter. The best-fit parameters are reported in Appendix C and are defined as the median of these posterior distributions. The quoted uncertainties correspond to the 16th and 84th percentiles. The corner-plots, such as the one shown in Figure 3 for M31, present the posterior probability density estimated by the MCMC. In the diagonal, the panels show the probability distributions of each parameter, while other panels exhibit the joint distributions between parameters, highlighting some degeneracies.

5. Results

We present the results for each galaxy in the sample: M31, LMC, SMC, M33, NGC 253, and NGC 4945. The following subsections describe the parameters derived for each galaxy, with the observed integrated SEDs and the corresponding best-fit models (Figures 2, 4, 5, and 6), together with the corner plots showing the parameter probability distributions. Best-fit parameters are listed in Table C.1.

5.1. M31

M31 is a well-detected galaxy across all photometric bands, extensively studied even in the mm–cm domain, and is the only nearby galaxy where the AME was detected on the integrated SED (Planck Collaboration Int. XXV 2015; Battistelli et al. 2019; Harper et al. 2023; Fernández-Torreiro et al. 2023a). We therefore used the results obtained for this galaxy as a detailed example and to check the reliability and advantages of our methodology.

The observed SED integrated in the region of M31 is presented in Figure 2 in gray points. The curves corresponding to the best fit model with the individual emission components are overlaid (best fit parameters are listed in Table C.1). Because our interest lies in the emission from the galaxy itself, we removed

¹⁰ $C_{\text{syn}} \in [0, 700]$ and $\delta_{\text{CMB}} \in [-50, 100]$ μK for the LMC.

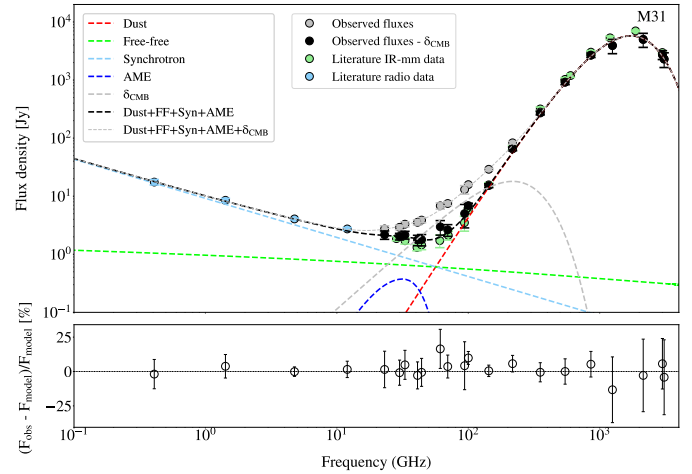


Fig. 2. Integrated SED of M31. The gray points represent the flux densities of the galaxy with the CMB fluctuations in the background. This SED was fit with our model, together with the radio data from the literature (blue points). The black points correspond to the flux densities of the galaxy from which the CMB fluctuations were subtracted from the values obtained with the best model of δ_{CMB} . The different emission components of our model obtained for the best fit are also represented. The blue points correspond to radio data from the literature. The green points correspond to literature data from Fritz et al. (2012); Bennett et al. (2013); Planck Collaboration Int. XXV (2015). The bottom panel shows residuals between the observed and modeled flux densities of M31.

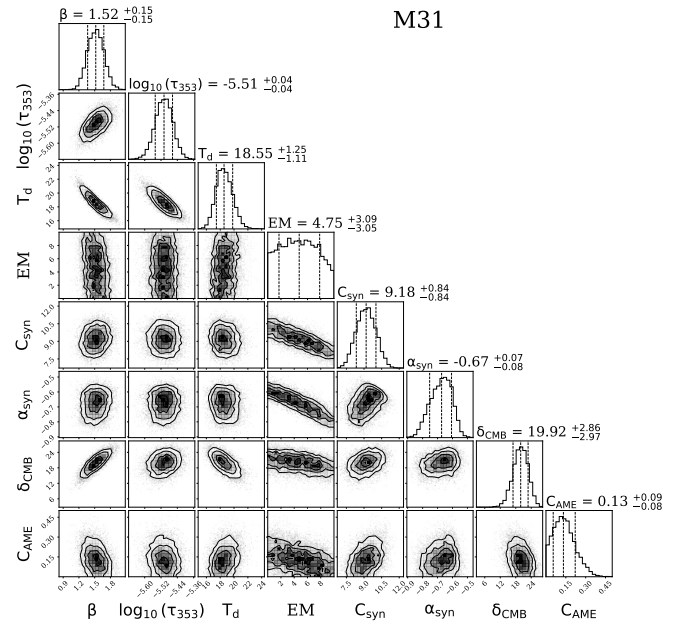


Fig. 3. Posterior probability distributions for each free parameter of the model for the SED of M31. The values of the best-fit parameters obtained with the MCMC are written above each histogram.

the δ_{CMB} fluxes obtained from the best fit model and overlaid the resulting SED of the galaxy alone with black points.

As seen in the right panel of Figure 2, our simple model is enough to reproduce the emission observed within the uncertainties. With the data set we have, we find that we do not need any break in the dust emissivity index and a simple modified black-body is enough to reproduce the thermal dust emission. This could result from the large spatial scales examined and the large uncertainties in the DIRBE fluxes, which influence the shape of

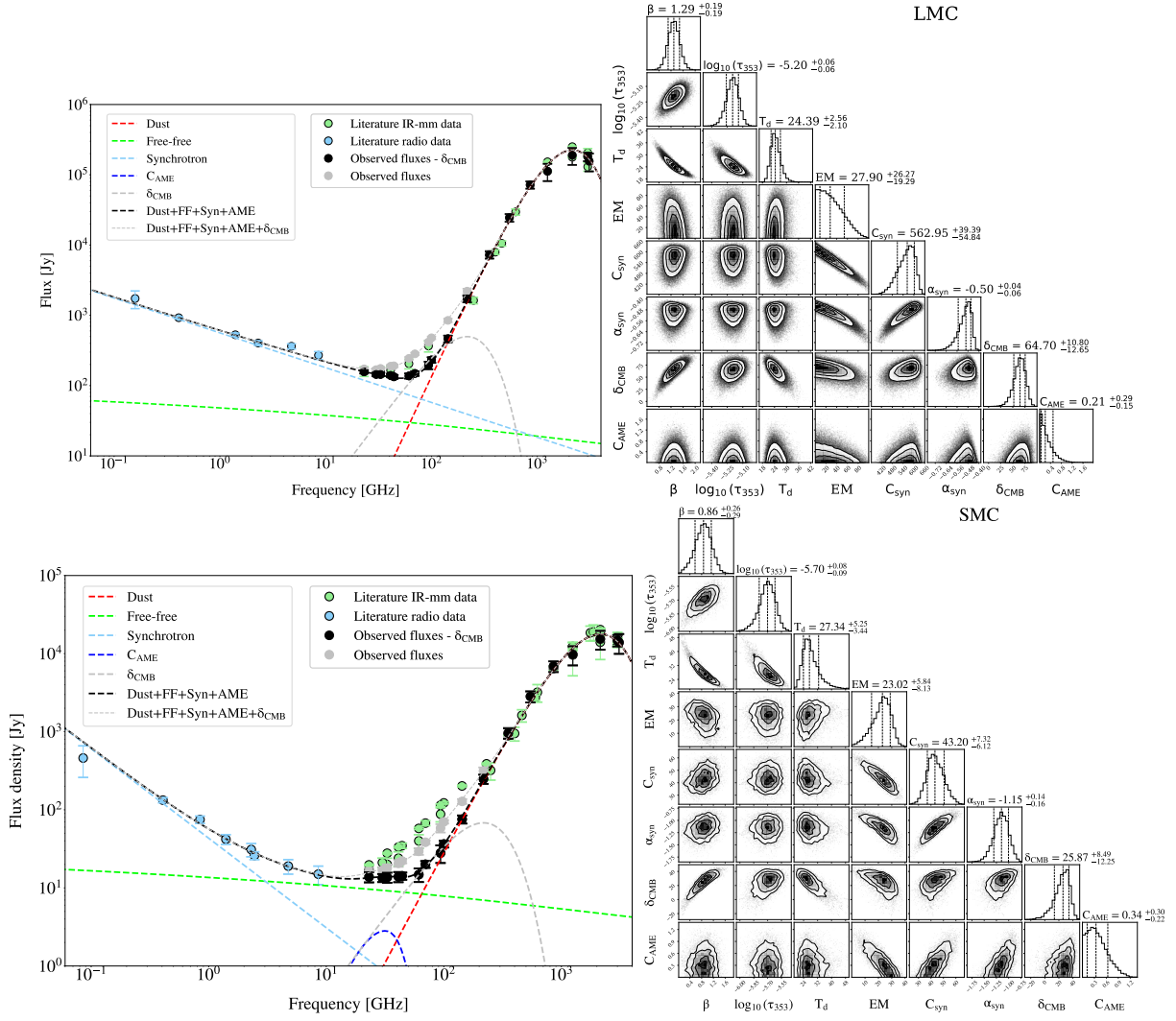


Fig. 4. SEDs of the LMC (top) and SMC (bottom) as observed with gray points and without the CMB with black points (subtracted from the best model), and radio data in light blue (from Table A.1 for the LMC and Table A.2 for the SMC). The data points from the literature (Israel et al. 2010; Planck Collaboration XVII 2011) are overlaid in green. The best-fit model spectra are overlaid for the global model and individual emission components. On the right, the corner plot displays probability distributions of each free parameter of the models. The values of the best-fit parameters obtained with the MCMC are written above each histogram.

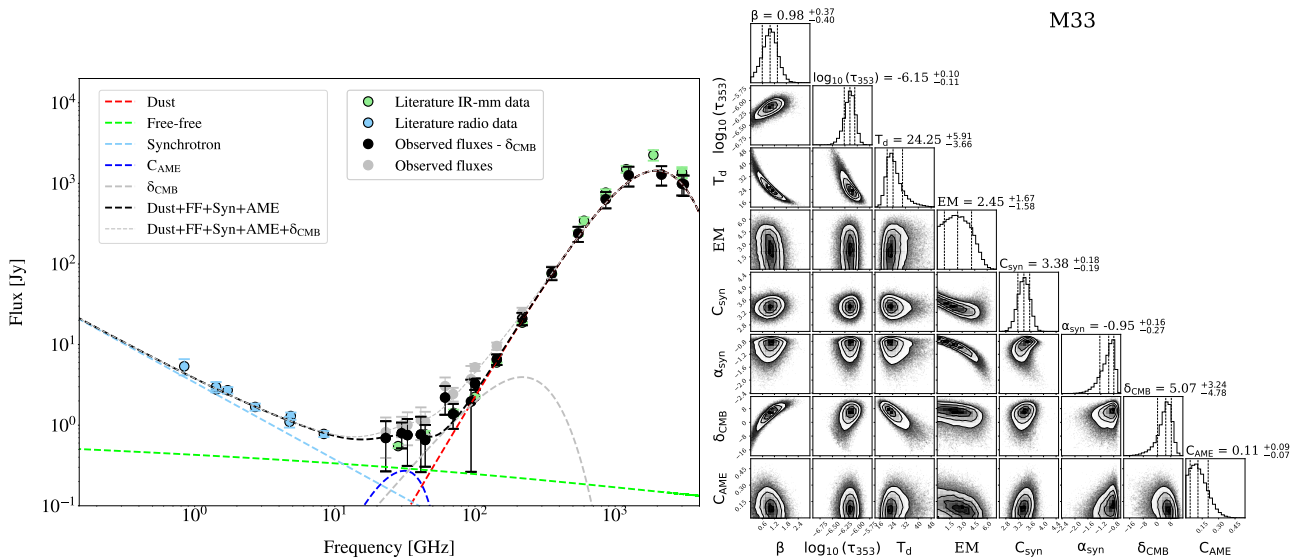


Fig. 5. Same as Figure 4 for M33. IR literature data are overlaid in green (Tibbs et al. 2018), and radio data in light blue (from Table A.4).

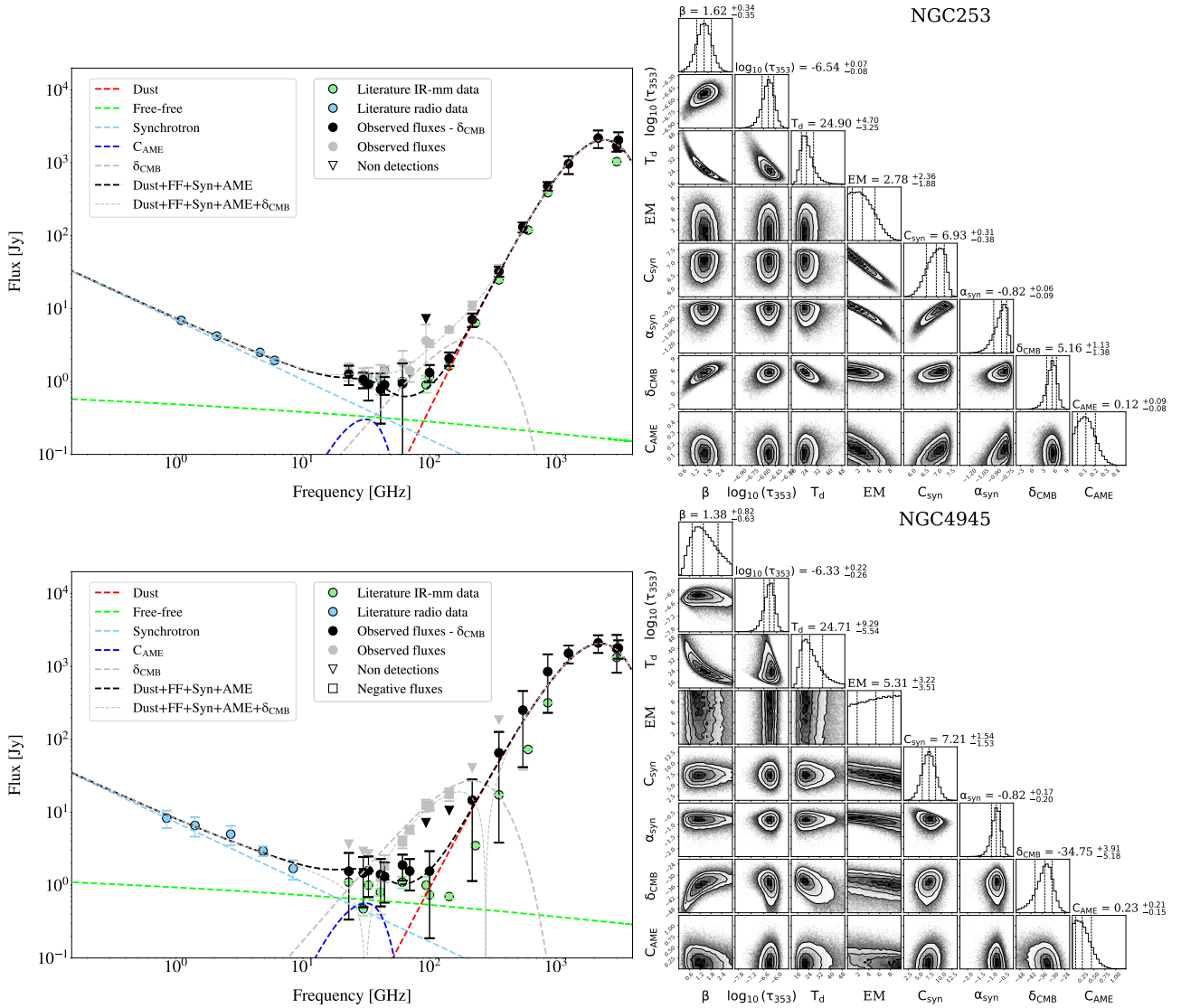


Fig. 6. Same as Figure 4 for NGC 253 (top), and NGC 4945 (bottom). Negative values are plotted as squares, using the absolute values of the measured flux densities. Non-detections are represented by upside-down triangles. IR literature data are overlaid in green (Clark et al. 2018), and radio data in light blue (from Tables A.5 for NGC 253 and A.6 for NGC 4945).

the IR peak. The best fit parameters we obtained for dust emission correspond to an emissivity index $\beta = 1.52 \pm 0.15$ and a dust temperature T_d of 18.5 ± 1.17 K. This is consistent with results derived previously (Planck Collaboration Int. XXV 2015; Fernández-Torreiro et al. 2023a; Harper et al. 2023)¹¹.

Analyzing the probability distributions of our model parameters (Figure 3), we first observe the well-known and strong anti-correlation between the thermal dust parameters β and T_d due to the degeneracies between them in the simple modified blackbody model for thermal dust (Dupac et al. 2003; Shetty et al. 2009; Ysard et al. 2012). This degeneracy is amplified by the uncertainties we have in all bands. Most of these uncertainties are mainly driven by imperfections in the foreground and background subtractions and are known to be correlated between bands. Taking the correlation of uncertainties into account could

reduce the degeneracies between our dust parameters (Gordon et al. 2014). This is not the main focus of this study and is postponed to further work. We do however keep the full probability distribution of β and T_d for each galaxy when comparing these parameters between galaxies, as these degeneracies are distinct yet superimposed on actual $T_d - \beta$ variations (see Section 5.6.3).

We also observe a clear degeneracy between β and δ_{CMB} . This is expected as β drives the slope of the long wavelength dust emission and an increase of positive δ_{CMB} in the background of a galaxy may mimic a flatter spectral shape in the millimeter regime. This is exactly what we observe in the $\delta_{\text{CMB}} - \beta$ joined probability distribution for M31. Within the uncertainties, the SED of M31 can be reproduced similarly with a steeper dust emissivity and a higher CMB fluctuation in the background, or a shallower dust emissivity and a lower positive CMB fluctuation in the background of this galaxy. For M31, flux densities are however sufficiently bright that both parameters can be detected significantly despite this correlated uncertainty.

Finally, we observe a degeneracy between the free-free and synchrotron parameters, hindering a precise determination of

¹¹ Planck Collaboration Int. XXV (2015) found $\beta = 1.62 \pm 0.11$ and $T_d = 18.2 \pm 1.0$ K; Fernández-Torreiro et al. (2023a) deduced $\beta = 1.71 \pm 0.08$ and $T_d = 18.5 \pm 0.79$ K; Harper et al. (2023) obtained $\beta = 1.44 \pm 0.09$ and $T_d = 19.1 \pm 0.8$ K.

the free-free emission level in our analysis. As we can see in Figure 3, the uncertainty on the free-free parameter EM is very large and we only measure an upper limit. The synchrotron spectral index we obtain ($\alpha_{\text{syn}} = -0.67 \pm 0.07$) is consistent with the one obtained by Harper et al. (2023) (-0.66 ± 0.03) and Fernández-Torreiro et al. (2023a) (-0.97 ± 0.21), yet lower than values obtained by Planck Collaboration Int. XXV (2015) (-0.92 ± 0.16) or Battistelli et al. (2019) (-1.1 ± 0.1). These differences can be attributed to the radio flux densities used in the different studies and in particular the change obtained with the C-BASS measurement (Harper et al. 2023) that increased the M31 flux density at 4.76 GHz by a factor of ~ 2 by including extended radio emission.

M31 is currently the only nearby galaxy where AME was detected in the integrated SED (Planck Collaboration Int. XXV 2015; Battistelli et al. 2019; Harper et al. 2023; Fernández-Torreiro et al. 2023a). However, the significance of the detection and amplitude of the AME varies between studies, in particular in view of the change in the radio flux densities with C-BASS observations, as mentioned above, but also depending on the way in which CMB fluctuations were taken into account in the line of sight of this galaxy. In this context, Harper et al. (2023) investigated in detail how different treatments of the CMB affect the derived properties of M31 by testing several Planck CMB component-separation maps. Their analysis showed that the flux density associated with the CMB component is typically 0.2–0.3 Jy at 30 GHz, with a scatter of about 0.1 Jy, highlighting that the choice of CMB model or subtraction method can significantly influence the inferred amplitudes of the other emission components. For instance, Planck Collaboration Int. XXV (2015) reported an AME amplitude of 0.7 ± 0.3 Jy at 30 GHz, Battistelli et al. (2019) obtained 1.45 ± 0.18 Jy, Harper et al. (2023) derived 0.27 ± 0.09 Jy, and Fernández-Torreiro et al. (2023a) found a greater AME amplitude using the SMICA map (1.17 ± 0.29 Jy) compared to COMMANDER map (0.92 ± 0.34 Jy), degrading from a 4σ to a 2.7σ detection. The larger discrepancies are due to differences in CMB treatment and in the inclusion of flux from large-scale measurements such as C-BASS detection.

In our analysis, using a consistent modeling approach where CMB fluctuations are fit simultaneously with the galaxy emission components, we find an AME amplitude of 0.13 ± 0.08 Jy at 30 GHz. This corresponds to a detection significance of only 1.5σ , i.e., AME is not significantly detected. Among all results, Battistelli et al. (2019) and Fernández-Torreiro et al. (2023a) report the highest AME amplitude. However, Planck Collaboration Int. XXV (2015) and Harper et al. (2023) results are consistent with ours to better than 2σ , and they agree overall when the uncertainties are accounted for. Figure 3 shows that the strength of the AME in our modeling is slightly degenerate with the δ_{CMB} , but also with the free-free and the synchrotron emission. Globally, with our results, AME appears too faint to be detected in comparison to other components at the same wavelengths and our measured uncertainties.

This in depth analysis of M31 in comparison of previous studies supports our modeling choices and highlights the importance to be aware of degeneracies between model parameters, not only between the emission components (β - T_d or between the synchrotron and free-free emission) but also with the CMB fluctuations in the background.

5.2. The Magellanic Clouds

The SEDs of the Magellanic Clouds are well reproduced by our model, with dust emissivity indices of $\beta = 1.29 \pm 0.18$

for the LMC and a notably low $\beta = 0.86 \pm 0.27$ for the SMC. Planck Collaboration XVII (2011) reported steeper values ($\beta = 1.48 \pm 0.25$ for the LMC and $\beta = 1.21 \pm 0.27$ for the SMC). In contrast, we find higher dust temperatures than those derived by Planck Collaboration XVII (2011), who obtained $T_d = 21.0 \pm 1.9$ K for the LMC and $T_d = 22.3 \pm 2.3$ K for the SMC, while we derived $T_d = 24.4 \pm 2.33$ K and $T_d = 27.3 \pm 4.3$ K, respectively. For the SMC, the AME is only marginally detected, with $C_{\text{AME}} = 0.34 \pm 0.25$ Jy, and not detected in the LMC with $C_{\text{AME}} = 0.21 \pm 0.20$ Jy.

5.3. M33

We derived a particularly low $\beta = 0.98 \pm 0.37$ and a warmer T_d of $24.2 \text{ K} \pm 4.69$ compared to previous studies from Tibbs et al. (2018) where CMB fluctuations were subtracted from the maps. For the radio emission, we derived $C_{\text{syn}} = 3.38 \pm 0.18$ and $\alpha_{\text{syn}} = -0.95 \pm 0.21$. In comparison, Tibbs et al. (2018) constrained C_{syn} while allowing α_{syn} to vary freely, obtaining $\alpha_{\text{syn}} = -1.03 \pm 0.03$, which is slightly steeper than the value derived in this work. In the mm, the AME detection is marginal, with $C_{\text{AME}} = 0.11 \pm 0.08$ Jy, peaking at 31 GHz, indicating AME is a minor component at 1.4σ in the integrated SED.

5.4. NGC 253

For NGC 253, both the dust spectral index and temperature are lower and warmer, respectively, than previously reported in Peel et al. (2011). We found $\beta = 1.62 \pm 0.34$ and $T_d = 24.9 \text{ K} \pm 3.97$, while Peel et al. (2011) derived $\beta = 1.96 \pm 0.11$ and $T_d = 22.6 \text{ K} \pm 1.3$, but in the case where CMB fluctuations were subtracted from the maps. For the radio emission, we derived $C_{\text{syn}} = 6.93 \pm 0.34$ and $\alpha_{\text{syn}} = -0.82 \pm 0.07$, whereas Peel et al. (2011) reported $C_{\text{syn}} = 11.1 \pm 4.3$ and $\alpha_{\text{syn}} = -1.59 \pm 0.35$. Our results indicate a lower synchrotron coefficient and a flatter spectral index, reflecting the differences in the datasets, frequency coverage, and the treatment of CMB and other components in the modeling. For the AME emission, while Peel et al. (2011) found a 3σ upper limit of 0.14 Jy, while we found $C_{\text{AME}} = 0.12 \pm 0.08$ Jy peaking at 31 GHz.

5.5. NGC 4945

For NGC 4945, we obtained a dust spectral index and temperature of $\beta = 1.38 \pm 0.72$ and $T_d = 24.7 \pm 7.41$ K, respectively, which correspond to a lower β and higher T_d than the values reported by Peel et al. (2011) ($\beta = 2.5 \pm 0.2$ and $T_d = 18.9 \pm 1.1$ K), derived from maps where CMB fluctuations had been subtracted. In the radio domain, our measurements indicate a lower synchrotron normalization and a flatter spectral index than those reported by Peel et al. (2011). We measured $C_{\text{syn}} = 7.21 \pm 1.53$ and $\alpha_{\text{syn}} = -0.82 \pm 0.18$, while Peel et al. (2011) reported $C_{\text{syn}} = 12.3 \pm 3.1$ and $\alpha_{\text{syn}} = -1.15 \pm 0.20$. For the AME component, we found $C_{\text{AME}} = 0.23 \pm 0.18$ Jy, peaking at 31 GHz, whereas Peel et al. (2011) obtained only a 3σ upper limit of 0.13 Jy.

5.6. Comparing results for the whole sample of nearby galaxies

After we analyzed our sample of six galaxies in a consistent way, we describe below the results for all galaxies and what we can learn from the comparison between them.

5.6.1. CMB fluctuations in the background of our galaxy sample

We observe that for all our bright and nearby galaxies, the CMB fluctuations in the background are significant in the mm regime, accounting for 25.8% to 88% of the 100 GHz emission (galaxy + δ_{CMB}). The importance of this contribution is probably amplified by the 1° resolution adopted for this study. Indeed, this 1° scale corresponds also to the first and strongest peak seen in the power spectrum of the CMB temperature fluctuations. As highlighted by Planck Collaboration XV (2014), even bright Galactic sources can be affected by CMB fluctuations, leading to a small but generally positive bias in measured fluxes, particularly at frequencies below 100 GHz. Harper et al. (2023) extended this analysis to the galaxy M31, showing that the CMB can contribute a significant fraction of the total flux at microwave frequencies, and that fitting the CMB spectrally is often highly degenerate with other emission components such as free-free, AME, and synchrotron emission. While this is unfortunate and prevents us from detecting a wider sample of very nearby galaxies, it also means that higher resolution studies with instruments like the Sardinia Radio Telescope (Prandoni et al. 2017) or the Atacama Large Aperture submm/mm Telescope (Klaassen et al. 2020; Liu et al. 2024) will bring more insight on the mm–cm emission of galaxies. Nevertheless, nearby galaxies can cover very large areas on the sky, so observations must still map sufficiently large regions to properly account for both the galaxy emission and the background. Failing to do so can lead to missing a fraction of the total flux, which is particularly challenging at radio frequencies where instrumental and atmospheric effects limit accurate measurements of extended emission.

More surprisingly than the significance of CMB fluctuations towards the line-of-sight of galaxies, what is striking with our study is the fact that our modeling implies a positive CMB fluctuation in the background of five out of the six galaxies. Such positive fluctuations in the background were already reported individually in M31 (Planck Collaboration Int. XXV 2015; Fernández-Torreiro et al. 2023a; Harper et al. 2023) or in the LMC and SMC (Bot et al. 2010; Planck Collaboration XVII 2011). However, this is the first time that this is observed in a consistent way in a sample of nearby galaxies and the quasi systematic positive δ_{CMB} are clearly revealed. In Section 6 we discuss the significance of this effect.

5.6.2. The case of the SMC

For the SMC, we observe that the data points from previous studies (Israel et al. 2010; Planck Collaboration XVII 2011) are well above the gray points from our study, both being taken with CMB fluctuations kept in. The green points delineating a flat emissivity shape were the reasons for Bot et al. (2010) to claim the existence of a microwave excess above the expected emission. In Planck Collaboration XVII (2011), this excess was partly attributed to a positive CMB fluctuation in the background of the SMC and fully attributed to a positive CMB fluctuation in the background of the LMC. When comparing flux densities from Planck Collaboration XVII (2011) to the one we get (our black points), both with CMB fluctuations removed, both are however completely consistent despite the different methodology. We tracked down this puzzling inconsistency to the fact that our foreground subtraction is slightly different and that our background subtraction is done using maps where the CMB fluctuations have been removed. Surprisingly, in the annulus around the SMC where this background is estimated (both in

Planck Collaboration XVII 2011 and in this work) several negative CMB fluctuations are present in the CMB fluctuation maps from any component separation we have checked (including the COMMANDER map we use to remove the CMB fluctuations before estimating the background flux). The strong strength of the initial microwave excess reported by Bot et al. (2010) might hence be not only due to a positive CMB fluctuation in the background of the SMC but also the subtraction of negative CMB fluctuations in the surrounding of the SMC. It is worth noting that systematic colder CMB temperatures have been highlighted to appear in the surrounding of galaxies (Hansen et al. 2023; Luparello et al. 2022; Lambas et al. 2024), potentially tracing an unaccounted CMB foreground that could also exist in the SMC as well. It is also possible that the scale of the SMC and of the background annulus correspond unfortunately to a peak and a trough of the CMB temperature fluctuation power spectrum, a situation that will tend to favor an anti-correlation between the CMB temperature fluctuations observed at these scales. This possibility was raised in Ferraro & Hensley (2015) who computed a formalism to estimate the impact of CMB fluctuations in aperture photometric measurements. Analyzing the occurrence of CMB fluctuations in the background or surrounding of galaxies in a larger sample is therefore required to go further and is discussed in the context of our small sample in section 5.6.1.

5.6.3. Dust properties

The dust thermal emission parameters we obtain for our sample of galaxies show large variations. While M31 is well described with dust emission with an emissivity index $\beta = 1.52 \pm 0.15$ similar to our Milky Way (1.60 ± 0.06 ; Planck Collaboration XIV 2014), M33 and SMC are distinguished by a particularly low β of 0.98 ± 0.37 and 0.86 ± 0.27 respectively. Even accounting for the large uncertainties, these values are much lower than the dust emissivity index observed for thermal dust emission in our solar neighborhood. Although slightly higher, we also find a low β of 1.29 ± 0.18 for the LMC. Such low emissivity index (even to just phenomenologically describe dust emission) in galaxies can be due to a combination of effects: (1) mixing of temperatures with larger amounts of colder dust (Galliano et al. 2003; Paradis et al. 2009); (2) different dust grain composition (Paradis et al. 2010); (3) a flattening of the intrinsic dust emissivity (Coupeaud et al. 2011) or effects in amorphous solids (Meny et al. 2007); or 4) magnetic dipole emission at long wavelengths (Draine & Hensley 2012). These low β values are the same phenomenology as large submm excess as reported in galaxies (e.g., Galametz et al. 2011; Rémy-Ruyer et al. 2013; Galliano 2022) obtained with models that include a fixed and shallower emissivity index (e.g., $\beta = [1.5-2]$). These low- β , submm excess or flat dust emission have been reported already in M33 and SMC (Galliano et al. 2003; Bot et al. 2010; Planck Collaboration XVII 2011; Paradis et al. 2012; Galliano et al. 2018; Tibbs et al. 2018) and are more widely observed in dwarf galaxies, low metallicities or regions of low densities (Rémy-Ruyer et al. 2013; Galliano et al. 2018). More recent work by Paradis et al. (2024) also reports similarly low values of β ($= 1$, and defined as the slope between $850 \mu\text{m}$ and 1.38 mm), in Galactic and nearby galaxy environments, from neural-network-based predictions of dust emission maps at submm–mm wavelengths, further supporting the picture of a flat dust emission spectrum at long wavelengths. Given the β - δ_{CMB} degeneracy discussed in Section 5.6.1, getting higher β values with our model would be possible but would imply even higher positive δ_{CMB} than currently reported.

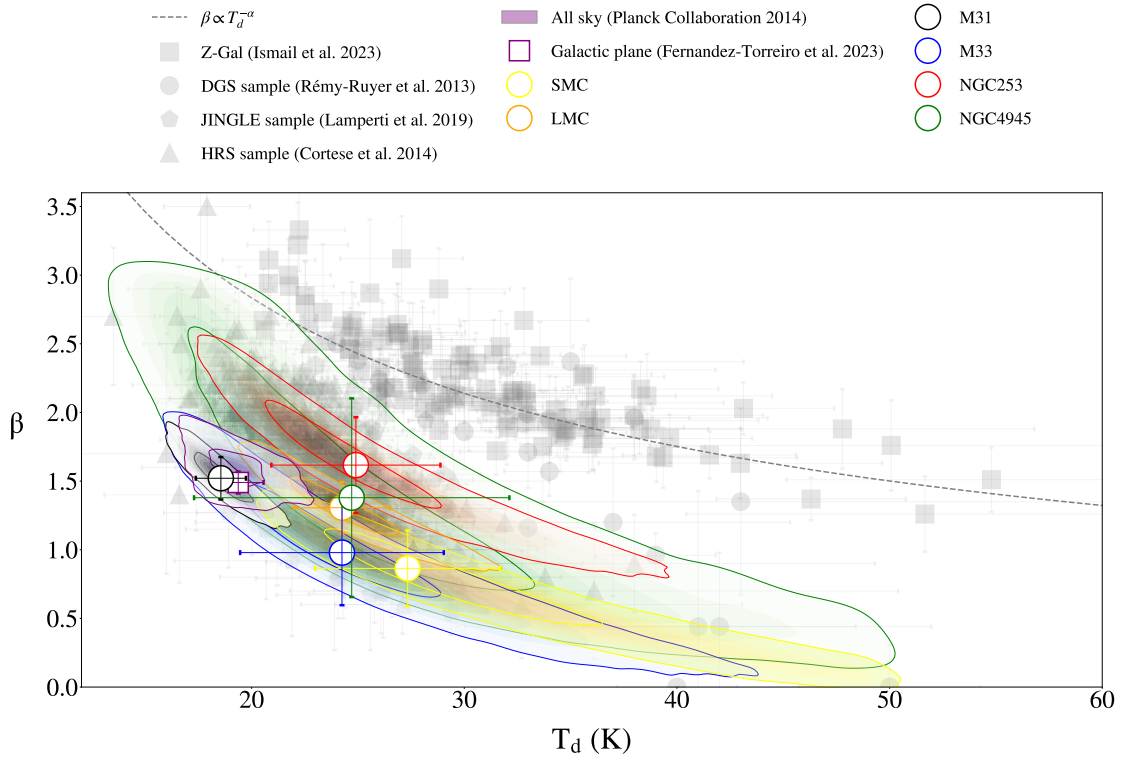


Fig. 7. Comparison between the dust parameters β and T_d for the six galaxies. The variations we observed are compared to the same parameters as obtained for other environments: the all-sky survey of *Planck* (Planck Collaboration XI 2014), the Milky Way (Fernández-Torreiro et al. 2023b), dwarf galaxies (Rémy-Ruyer et al. 2013), nearby galaxies from the *Herschel* Reference Survey (Cortese et al. 2014) and for high-redshift galaxies from Ismail et al. (2023).

Degeneracies between β and T_d are clearly seen in all probability distributions obtained with our modeling (see Figures 3, 4, 5, and 6). Despite these, intrinsic dust property changes are also observed beyond these degeneracies. We compare in Figure 7 our best fit β and T_d values for the six nearby galaxies analyzed in this work. We observe that the β values deduced are significantly different between our six galaxies, hence showing actual variations of the dust thermal emission slope between these galaxies. We observe a trend of lower β values for higher dust temperatures, even if this trend is difficult to disentangle from the degeneracy between the two parameters. This anti-correlation has been widely reported in both observational and theoretical works (e.g., Désert et al. 2008; Paradis et al. 2010; Smith et al. 2012; Juvela et al. 2013; Kirkpatrick et al. 2014; Cortese et al. 2014), and more recently in high-redshift studies such as in Ismail et al. (2023). This β - T_d relation could reflect both the intrinsic properties of interstellar dust grains and the physical characteristics of the environments in which they reside. Such an inverse dependency has also been observed in laboratory experiments of interstellar grain analogs, including both amorphous carbons and silicates (Agladze et al. 1996; Mennella et al. 1998; Demyk et al. 2017).

For comparison, we include in Figure 7 results from other studies in different galaxy samples: dwarf galaxies from the DGS sample (Rémy-Ruyer et al. 2013), more massive systems from the *Herschel* Reference Survey (Cortese et al. 2014), main sequences galaxies from the JINGLE survey (Lamperti et al. 2019), high-redshift galaxies from Ismail et al. (2023), and for the Galactic plane from Fernández-Torreiro et al. (2023b). The results we obtained for our sample are globally consistent with the general trends observed at higher resolution with

other local galaxies, including the Milky Way. As reported in Ismail et al. (2023), galaxies at high redshift display a similar decreasing β with increasing T_d yet is shifted to systematically higher β for a given dust temperature. In our sample, we observe that the starburst galaxy NGC 253 also appear shifted (although less than high- z galaxies) with respect to local group galaxies in our sample (LMC, SMC, M31, M33). All galaxies are however broadly compatible with other galaxy samples in our nearby universe (Rémy-Ruyer et al. 2013; Cortese et al. 2014; Lamperti et al. 2019). These differences in the long wavelength shape of dust in galaxies could be related to differences in ISM conditions, such as variations in radiation field intensity, dust grain growth, or changes in dust composition. A lower β might indicate larger or more processed grains, while higher temperatures in high-redshift galaxies could be associated with stronger star formation activity and a more intense interstellar radiation field. Whatever the physical processes at stake, these results confirm that dust properties depend on the environment and vary between galaxies.

5.6.4. Anomalous microwave emission

The detection of AME in M33, NGC 253, NGC 4945, and SMC is marginal. Our best fit parameters for the AME flux densities are summarized in Table C.1 and the probability distribution functions obtained are visible in Figures 3, 4, 5, and 6. We only found a small correlation between the AME parameter, C_{AME} , and the free-free parameter EM, and not a visible correlation with the other parameters, meaning that AME is relatively independent of the other components, yet it seems to be a very minor component of the integrated emission of the galaxy. Comparing the models with and without the AME component

(values summarized in Table C.1), the parameters change only modestly and remain consistent within their uncertainties. The inclusion of AME results in only minor reductions in χ^2 for few galaxies (SMC, M31, and NGC 253), while in some galaxies (LMC, M33, and NGC 4945) the fit is even slightly degraded. Overall, these results indicate that AME is a minor contributor to the integrated emission. Since AME has been more clearly detected in individual well resolved extragalactic regions (Murphy et al. 2010; Hensley et al. 2015; Murphy et al. 2018), this systematic non-detection of AME in all galaxies of our sample might arise because it is only a significant process in specific regions of galaxies and not visible in integrated SED due to the dilution of this component on large-scales.

One can wonder whether our non-detection are consistent with what would be expected from the dust emission observed in these galaxies. To do this, we expressed our AME best-fit components into AME emissivities. The AME emissivity is defined in Fernández-Torreiro et al. (2023b) as the ratio of the AME intensity at its peak frequency and the thermal dust intensity at 3000 GHz (100 μm),

$$\epsilon_{\text{peak}}^{\text{AME}} = \frac{T_{\text{peak}}^{\text{AME}}}{I_{3000 \text{ GHz}}} = \frac{c^2}{2k_B v^2} \frac{S_{\text{peak}}^{\text{AME}}}{S_{3000 \text{ GHz}}}. \quad (8)$$

We used the AME emissivity to normalize the AME by dust content, enabling meaningful comparison of its strength across regions with different dust amounts.

The AME emissivities computed from our best fits for our sample of galaxies are given in Table C.1. Our derived upper limits on $\epsilon_{\text{peak}}^{\text{AME}}$ are lower than typical values observed in our Galaxy of 10–14 $\mu\text{K}/(\text{MJy}/\text{sr})$ (Davies et al. 2006; Planck Collaboration XXIII 2015; Harper et al. 2022; Fernández-Torreiro et al. 2023b). This confirms that the AME component in our integrated sample of galaxies is weak compared to Galactic standards. To account for the sensitivity of 3000 GHz-based emissivities to dust temperature variations (e.g., Tibbs et al. 2012), we also computed the AME emissivity normalized by the optical depth at 353 GHz τ_{353} . Using this normalization, we obtain values of $5.94 \pm 0.69 \text{ K}/\tau_{353}$ for M31, $34.13 \pm 10.70 \text{ K}/\tau_{353}$ for M33, $86.67 \pm 20.28 \text{ K}/\tau_{353}$ for NGC 253, $53.14 \pm 33.20 \text{ K}/\tau_{353}$ for NGC 4945, $3.85 \pm 0.64 \text{ K}/\tau_{353}$ for the LMC, and $13.72 \pm 3.47 \text{ K}/\tau_{353}$ for the SMC. The difference between our 3000 GHz- and τ_{353} -normalized emissivities reflects the sensitivity of the 3000 GHz emission to dust temperature. Even modest variations in dust temperature can strongly affect the measured brightness, leading to systematically lower and more scattered emissivities, while normalization by longer-wavelength tracers better accounts for residual temperature variations. These τ_{353} emissivity results suggest that AME, while present, is a minor contributor to the integrated emission of these galaxies, consistent with our earlier conclusion based on the marginal detections. However, the relatively higher emissivities in M33, NGC 253, and NGC 4945 might indicate that AME is more prominent in specific regions or environments with favorable physical conditions, such as dense gas or strong radiation fields, even when the integrated galaxy signal remains low. These findings align with Galactic studies and extragalactic work, highlighting that AME is strongest in localized environments and can be diluted when averaging over whole galaxies (Tibbs et al. 2012; Planck Collaboration XI 2014; Dickinson et al. 2018; Bianchi et al. 2022), although our measured value for M31 is higher than the one reported by Harper et al. (2023). AME is probably not a dominant emission component at the scale of a whole galaxy and may only be significant in localized environments where physical conditions favor spinning

dust emission. Since specific physical conditions are required to excite efficiently (Draine & Lazarian 1998b), it might not be surprising that spinning dust emission would be concentrated in dense regions or environments where the radiation field is intense (Tibbs et al. 2013; Hermelo et al. 2016). Thermal dust emission at high frequencies reflects the overall dust distribution heated by ambient radiation, while AME originates from specific grain populations localized in certain regions. As a result, averaging AME emissivity over large areas dilutes the signal due to regions with little or no AME, producing our observed low average values. Although detecting AME in the integrated spectra of galaxies remains challenging, it can serve as a tracer of the relative contribution of dense regions within galaxies. In particular, AME detections have been reported in some galaxies where conditions favor significant small grain rotation, such as a star-forming region in NGC 6946 (first extragalactic detection; Murphy et al. (2010); Hensley et al. (2015) and a compact radio source associated with NGC 4725 (Murphy et al. 2018). Since higher resolution observations or redshifted SEDs of more distant galaxies will be less impacted by the CMB fluctuations in the background, there is an interest in continuing the search for extragalactic AME, either in resolved regions within nearby galaxies or in integrated SEDs of more distant galaxies.

5.6.5. Free-free emission

In our model, the free-free emission is parametrized with the emission measure EM. The best fit parameters obtained for all galaxies are summarized in Table C.1. Except for the SMC where free-free emission is clearly detected, we find that the integrated SEDs of our sample of galaxies are reproduced with subdominant free-free emission. EM is often poorly constrained in our study. The large uncertainties stem both from the degeneracies between the synchrotron, AME emissions and CMB anisotropies, as we can see in Figures 3, 4, 5, and 6, and from the relatively low contribution of the galaxy flux densities at long wavelengths, where the synchrotron and CMB components dominate. The inverse correlation we observe in the probability distribution between the synchrotron strength and slope and the free-free emission strength could potentially be solved with priors on the physical processes that drive an actual correlation between these two components. Indeed, thermal and nonthermal emission processes can be associated with star formation in galaxies and known to be connected on large scales (e.g., Tabatabaei et al. 2013a,b). However, the strength of these physical correlations is nontrivial and it can vary depending on the spatial scale and the physical conditions of the interstellar medium and the structure of magnetic fields.

6. Discussion

6.1. Assessing the effect of CMB fluctuations

Our modeling infers a positive δ_{CMB} in five out of six galaxies which is surprising. The significance of this quasi-systematic positive δ_{CMB} in the background of our sample of galaxies can be examined by estimating the probability of observing at least five positive fluctuations among six galaxies using a binomial distribution. Under the assumption that CMB temperature fluctuations are randomly distributed following a symmetric Gaussian distribution centered on zero, the resulting probability we compute is $\approx 9.4\%$, which is not formally significant. However, we also need to take into account the amplitudes of the δ_{CMB} we infer from

our modeling, as several are substantially larger than their associated uncertainties. The mean of the six δ_{CMB} inferred values is $14.32 \mu\text{K}$, which is inconsistent at 5.03σ with a null expectation when the individual errors are taken into account. From that perspective, the δ_{CMB} in the background of our sample of galaxies are therefore very significant.

However, CMB temperature fluctuations have very specific spatial distributions that are shown as clear peaks in the CMB fluctuation power spectrum. In order to evaluate the statistical relevance of our δ_{CMB} , with respect to the expected variations of δ_{CMB} on the sky, we performed an MCMC analysis in which the CMB fluctuations were sampled at six random positions on the sky, using the same apertures as described in Section 3.3. For each realization, the mean flux density over the six apertures was computed, and the procedure was repeated 1000 times. The resulting distribution of mean values is centered on zero with a standard deviation of $\approx 47 \mu\text{K}$, which is much larger than our average $\langle \delta_{\text{CMB}} \rangle \approx 15 \mu\text{K}$. Although the fact that five out of six individual values are positive may appear noteworthy, especially given the significance of the δ_{CMB} values we infer from our modeling, in the context of the CMB variance such a configuration remains probable at these angular scales. This analysis indicates that the observed mean is not statistically distinguishable from what would be expected due to random CMB fluctuations.

Unexpected δ_{CMB} effects have been reported in larger galaxy samples (Luparello et al. 2022; Hansen et al. 2023; Lambas et al. 2024). Put in this context, our quasi systematics positive δ_{CMB} might trace a similar effect in local galaxies. Yet, our positive δ_{CMB} are currently not significant given the CMB variance to confirm and disprove such effect in nearby galaxies. To go further, it will hence require to extend the study to a much larger sample of galaxies, and/or data at higher resolution.

The case of the SMC where negative fluctuations of CMB temperatures are present in the surroundings, while a positive CMB temperature fluctuation is inferred from our modeling of the observed emission towards the line-of-sight of the SMC itself, adds to this questioning. The low β for the dust emission and the β - δ_{CMB} degeneracy also need to be better understood to improve our knowledge on these effect. More work is clearly needed especially at high angular resolution where we can expect intrinsically lower fluctuations of the CMB temperature. This would help to understand both this potential new CMB foreground component and the dust emission at long wavelengths.

6.2. Variability in the AME peak frequency

It is well established that in Galactic PDRs, the AME peak can shift toward mm wavelengths, (e.g., Casassus et al. 2008; Tibbs et al. 2010, 2011; Scaife et al. 2010; Bell et al. 2019; Cepeda-Aroita et al. 2021) where the peak position is found to vary with local physical conditions (Ysard et al. 2022). Moreover, Poojon et al. (2024) found that AME was detected in NGC 2903 and marginally in NGC 2146, with the spinning dust emission peaking at higher frequencies and showing stronger emissivity than previously reported. This supports the spinning dust model prediction that AME peaks shift to higher frequencies in denser environments, such as molecular clouds and PDRs. These results indicate that the AME peak frequency is not fixed, and raises the possibility that part of the mm excess observed in galaxies could be related to a shifted AME peak. However, the spectral shape of the excess emission we observed is already well reproduced by a combination of thermal dust emission, CMB fluctuations, free-free, and synchrotron emission. The CMB component is particularly difficult to reconcile

with a shifted AME spectrum. Testing such a scenario would require introducing additional free parameters, which would further increase degeneracies in the modeling. Indeed, studies that have attempted this approach often find very large shifts of the AME peak into the radio domain, raising questions about the physical plausibility of such solutions (Poojon et al. 2024).

6.2.1. Limitations of the radio data

In our analysis, we incorporate radio data compiled from the literature. A fully consistent treatment would require processing the radio measurements in the same way as the FIR-cm data to ensure homogeneity across the entire wavelength range, but this is beyond the scope of this study. While this is a weak point of our analysis, we believe this difference does not have an impact on the results. The use of radio data is needed, as these points provide constraints on the levels of free-free and synchrotron emission. Yet, the estimates do not need to be as accurate as in the FIR-mm to constrain the dust emission and δ_{CMB} . We perform tests in which we artificially increased the uncertainties of the radio data points. While this increase changed the free-free and synchrotron inferred values, it does not impact our conclusions on dust and δ_{CMB} . We present the case of the LMC analysis with increased radio uncertainties in Appendix D. The fits indicate an increase in the free-free emission component EM, whereas the contribution from δ_{CMB} shows only a marginal change. These tests confirm that our conclusions on CMB fluctuations are not solely driven by the uncertainties or potential biases in the radio measurements. Although the radio data available in the literature may carry significant uncertainties, they do not dominate the overall results of our fits.

7. Conclusion

We performed the first homogeneous analysis of six very nearby galaxies with an excellent wavelength coverage in the mm-cm domain. We used data from COBE-DIRBE, IRAS, *Planck*, and WMAP from $100 \mu\text{m}$ (3000 GHz) to 13 mm (22.8 GHz) at a resolution of 1° to study six nearby galaxies: M31, M33, NGC 253, NGC 4945, and the LMC and SMC. The global SED can be well represented by a model of dust, free-free, synchrotron, and AME emissions, with CMB temperature fluctuations in the background.

Our resulting parameters for the thermal dust emission, free-free and synchrotron are consistent with what has been seen in individual studies of these galaxies and previous results from the literature. We highlight the very low dust emissivity indices that were inferred to describe the dust emission of the SMC, M33, or the LMC, noting that these β values are purely phenomenological and do not reflect the actual intrinsic β values of dust in these galaxies. The comparison of our resulting dust parameters between galaxies showed significant variations in β and T_d between the galaxies. These variations are consistent with the variation that is observed in larger galaxy samples and can be compared to higher-redshift samples.

While AME is present in the best-fit models for all galaxies in our sample, the detections are marginal ($\leq 1\sigma$) in each case, with AME emissivities lower than typical Galactic standards. This shows that AME is a very minor component in the integrated spectra of these nearby galaxies, and this is consistent with previous studies. In M31, we measured an AME amplitude of $0.13 \pm 0.08 \text{ Jy}$ at 30 GHz (1.5σ), which is lower than earlier estimates, such as Battistelli et al. (2019), but consistent within

the uncertainties with [Planck Collaboration Int. XXV \(2015\)](#) and [Harper et al. \(2023\)](#). The differences between the studies largely reflect the inclusion of large-scale flux (e.g., C-BASS) and the treatment of CMB and free-free emission. These results confirm overall that AME is weaker than other emission components.

We emphasize that CMB fluctuations contribute significantly to the mm–cm flux at 1° resolution in all the galaxies we analyzed. Our results highlight a suspicious inferred presence of a quasi-systematic positive CMB temperature fluctuation in the background of five out of six galaxies. When the CMB variance is taken into account, this might reflect a statistical bias due to the small size of our sample and the particular 1° scale of our study. Further work is required to determine whether the δ_{CMB} effect observed in the background of more distant galaxies might also exist in the local galaxies we studied, and if it traces an unknown emission component that is not yet accounted for. Degeneracies between δ_{CMB} and the dust emissivity index β might play a role in changing the importance of these inferred positive CMB temperature fluctuations in the background of galaxies. However, we stress that a decreased δ_{CMB} in the background would flatten the inferred shape of the dust emission at long wavelengths even more. This possibility needs to be carefully assessed in light of current dust models.

Studies with a higher angular resolution are needed to understand the long-wavelength shape of dust emission in galaxies better and to use this knowledge to separate it from the CMB temperature fluctuations in the galaxy background and the surroundings, including with a potential new foreground component. Current upgrades of the Sardinia Radio Telescope ([Prandoni et al. 2017](#)), further QUIJOTE observations ([Génova-Santos et al. 2015](#)), or the Atacama Large Aperture Submillimeter Telescope ([Klaassen et al. 2020](#)) all hold the potential to study nearby galaxies in the mm–cm range in more detail, which would reduce the uncertainty due to CMB temperature fluctuations and would better separate foreground and background emission sources that currently dominate our uncertainties. The advent of large radio facilities such as the Square Kilometer Array (SKA; [Dewdney et al. 2009](#)) will drastically change our understanding of the thermal and nonthermal radio components in galaxies with its unprecedented detail. Furthermore, the rest-frame mm–cm emission of galaxies at redshifts 2 and higher will be observed with SKA-mid and might be detected, which would provide access to this long-wavelength thermal dust, AME, and to the free-free emission part of the galaxies, with any contributions from the CMB temperature fluctuations. These future facilities therefore hold strong promises for our understanding of the mm–cm galaxy emission.

Data availability

Maps of LMC, SMC, M33, NGC 253, and NGC 4945 before and after the subtraction of the foreground and background sources are available on the public platform [Zenodo](#).

Acknowledgements. We would like to thank M.-A. Miville-Deschênes and B. Hensley for insightful discussions at different stages of this work. We thank the referee for useful comments which helped improve the content of the paper.

References

Agladze, N. I., Sievers, A. J., Jones, S. A., Burlitch, J. M., & Beckwith, S. V. W. 1996, *ApJ*, **462**, 1026
 Ali-Haïmoud, Y., Hirata, C. M., & Dickinson, C. 2009, *MNRAS*, **395**, 1055
 Allison, J. R., Sadler, E. M., & Meekin, A. M. 2014, *MNRAS*, **440**, 696

Alvarez, H., Aparici, J., & May, J. 1989, *A&A*, **213**, 13
 Battistelli, E. S., Fatigoni, S., Murgia, M., et al. 2019, *ApJ*, **877**, L31
 Bell, A. C., Onaka, T., Galliano, F., et al. 2019, *PASJ*, **71**, 123
 Bendo, G. J., Dale, D. A., Draine, B. T., et al. 2006, *ApJ*, **652**, 283
 Bennett, C. L., Larson, D., Weiland, J. L., et al. 2013, *ApJS*, **208**, 20
 Bianchi, S., Murgia, M., Melis, A., et al. 2022, *A&A*, **658**, L8
 Bobin, J., Sureau, F., & Starck, J. L. 2016, *A&A*, **591**, A50
 Bot, C., Helou, G., Boulanger, F., et al. 2009, *ApJ*, **695**, 469
 Bot, C., Ysard, N., Paradis, D., et al. 2010, *A&A*, **523**, A20
 Boulanger, F., & Perault, M. 1988, *ApJ*, **330**, 964
 Boulanger, F., Abergel, A., Bernard, J. P., et al. 1996, *A&A*, **312**, 256
 Buczylowski, U. R. 1988, *A&A*, **205**, 29
 Cambresy, L., Reach, W. T., Beichman, C. A., & Jarrett, T. H. 2001, *ApJ*, **555**, 563
 Casassus, S., Dickinson, C., Cleary, K., et al. 2008, *MNRAS*, **391**, 1075
 Casassus, S., Vidal, M., Arce-Tord, C., et al. 2021, *MNRAS*, **502**, 589
 Cepeda-Arroita, R., Harper, S. E., Dickinson, C., et al. 2021, *MNRAS*, **503**, 2927
 Cheng, Y.-T., Hensley, B. S., Chang, T.-C., & Doré, O. 2025, *ApJ*, **985**, 15
 Chiang, I.-D., Sandstrom, K. M., Chastenet, J., et al. 2018, *ApJ*, **865**, 117
 Clark, C. J. R., Verstocken, S., Bianchi, S., et al. 2018, *A&A*, **609**, A37
 Clark, C. J. R., Roman-Duval, J. C., Gordon, K. D., Bot, C., & Smith, M. W. L. 2021, *ApJ*, **921**, 35
 Clark, C. J. R., Roman-Duval, J. C., Gordon, K. D., et al. 2023, *ApJ*, **946**, 42
 Compiègne, M., Verstraete, L., Jones, A., et al. 2011, *A&A*, **525**, A103
 Condon, J. J. 1992, *ARA&A*, **30**, 575
 Cortese, L., Fritz, J., Bianchi, S., et al. 2014, *MNRAS*, **440**, 942
 Coupeaud, A., Demyk, K., Meny, C., et al. 2011, *A&A*, **535**, A124
 Dale, D. A., & Helou, G. 2002, *ApJ*, **576**, 159
 Dale, D. A., Helou, G., Contursi, A., Silbermann, N. A., & Kolhatkar, S. 2001, *ApJ*, **549**, 215
 Davies, R. D., Dickinson, C., Banday, A. J., et al. 2006, *MNRAS*, **370**, 1125
 Demyk, K., Meny, C., Leroux, H., et al. 2017, *A&A*, **606**, A50
 Demyk, K., Gromov, V., Meny, C., et al. 2022, *A&A*, **666**, A192
 Désert, F. X., Macías-Pérez, J. F., Mayet, F., et al. 2008, *A&A*, **481**, 411
 Dewdney, P. E., Hall, P. J., Schilizzi, R. T., & Lazio, T. J. L. W. 2009, *Proc. IEEE*, **97**, 1482
 Dickinson, C., Ali-Haïmoud, Y., Barr, A., et al. 2018, *New Astr. Rev.*, **80**, 1
 Draine, B. T. 2011, *Physics of the Interstellar and Intergalactic Medium* (Princeton University Press)
 Draine, B. T., & Hensley, B. 2012, *ApJ*, **757**, 103
 Draine, B. T., & Lazarian, A. 1998a, *ApJ*, **494**, L19
 Draine, B. T., & Lazarian, A. 1998b, *ApJ*, **508**, 157
 Draine, B. T., & Li, A. 2001, *ApJ*, **551**, 807
 Draine, B. T., & Li, A. 2007, *ApJ*, **657**, 810
 Dupac, X., Bernard, J. P., Boudet, N., et al. 2003, *A&A*, **404**, L11
 Ejlali, G., Tabatabaei, F. S., Roussel, H., et al. 2025, *A&A*, **693**, A88
 Fernández-Torreiro, M., Génova-Santos, R. T., Rubiño-Martín, J. A., et al. 2023a, *MNRAS*, **527**, 11945
 Fernández-Torreiro, M., Rubiño-Martín, J. A., López-Caraballo, C. H., et al. 2023b, *MNRAS*, **526**, 1343
 Ferraro, S., & Hensley, B. 2015, *MNRAS*, **451**, 1606
 Finkbeiner, D. P. 2003, *ApJS*, **146**, 407
 Fixsen, D. J. 2009, *ApJ*, **707**, 916
 Foreman-Mackey, D., Farr, W. M., Sinha, M., et al. 2019, *J. Open Source Softw.*, **4**, 1864
 Fritz, J., Gentile, G., Smith, M. W. L., et al. 2012, *A&A*, **546**, A34
 Fullmer, L., & Lonsdale, C. J. 1995, *VizieR Online Data Catalog: Catalogued Galaxies + QSOs observed in IRAS Survey, Vers.2 (IPAC 1989)*, *VizieR Online Data Catalog: VII/113*. Originally published in: 1989IRASG....c....F
 Galametz, M., Madden, S. C., Galliano, F., et al. 2011, *A&A*, **532**, A56
 Galliano, F. 2018, *MNRAS*, **476**, 1445
 Galliano, F. 2022, arXiv e-prints [arXiv:2202.01868]
 Galliano, F., Madden, S. C., Jones, A. P., et al. 2003, *A&A*, **407**, 159
 Galliano, F., Galametz, M., & Jones, A. P. 2018, *ARA&A*, **56**, 673
 Génova-Santos, R., Rubiño-Martín, J. A., Rebolo, R., et al. 2015, in *Highlights of Spanish Astrophysics VIII*, eds. A. J. Cenarro, F. Figueras, C. Hernández-Monteagudo, J. Trujillo Bueno, & L. Valdivielso, 207
 Gordon, K. D., Roman-Duval, J., Bot, C., et al. 2014, *ApJ*, **797**, 85
 Górski, K. M., Hivon, E., Banday, A. J., et al. 2005, *ApJ*, **622**, 759
 Hansen, F. K., Boero, E. F., Luparello, H. E., & Garcia Lambas, D. 2023, *A&A*, **675**, L7
 Harper, S. E., Dickinson, C., Barr, A., et al. 2022, *MNRAS*, **513**, 5900
 Harper, S. E., Barr, A., Dickinson, C., et al. 2023, *MNRAS*, **523**, 3471
 Hauser, M. G., Arendt, R. G., Kelsall, T., et al. 1998, *ApJ*, **508**, 25
 Haynes, R. F., Klein, U., Wayte, S. R., et al. 1991, *A&A*, **252**, 475
 Hensley, B. S., & Draine, B. T. 2023, *ApJ*, **948**, 55
 Hensley, B., Murphy, E., & Staguhn, J. 2015, *MNRAS*, **449**, 809
 Hermelo, I., Lisenfeld, U., Relaño, M., et al. 2013, *A&A*, **549**, A70

- Hermelo, I., Relaño, M., Lisenfeld, U., et al. 2016, *A&A*, 590, A56
 HI4PI Collaboration (Ben Bekhti, N., et al.) 2016, *A&A*, 594, A116
 Ismail, D., Beelen, A., Buat, V., et al. 2023, *A&A*, 678, A27
 Israel, F. P., Wall, W. F., Raban, D., et al. 2010, *A&A*, 519, A67
 Jones, A. P., Fanciullo, L., Köhler, M., et al. 2013, *A&A*, 558, A62
 Jones, A. P., Ysard, N., Köhler, M., et al. 2014, *Faraday Disc.*, 168, 313
 Juvela, M., Montillaud, J., Ysard, N., & Lunttila, T. 2013, *A&A*, 556, A63
 Katsioli, S., Xilouris, E. M., Kramer, C., et al. 2023, *A&A*, 679, A7
 Kirkpatrick, A., Calzetti, D., Kennicutt, R., et al. 2014, *ApJ*, 789, 130
 Klaassen, P. D., Mroczkowski, T. K., Ciccone, C., et al. 2020, *SPIE Conf. Ser.*, 11445, 114452F
 Klein, U., Wielebinski, R., Haynes, R. F., & Malin, D. F. 1989, *A&A*, 211, 280
 Kogut, A., Banday, A. J., Bennett, C. L., et al. 1996, *ApJ*, 464, L5
 Köhler, M., Jones, A., & Ysard, N. 2014, *A&A*, 565, L9
 Köhler, M., Ysard, N., & Jones, A. P. 2015, *A&A*, 579, A15
 Lagache, G., Abergel, A., Boulanger, F., Désert, F. X., & Puget, J. L. 1999, *A&A*, 344, 322
 Lagache, G., Béthermin, M., Montier, L., Serra, P., & Tucci, M. 2020, *A&A*, 642, A232
 Lambas, D. G., Hansen, F. K., Toscano, F., Luparello, H. E., & Boero, E. F. 2024, *A&A*, 681, A2
 Lamperti, I., Saintonge, A., De Looze, I., et al. 2019, *MNRAS*, 489, 4389
 Leitch, E. M., Readhead, A. C. S., Pearson, T. J., & Myers, S. T. 1997, *ApJ*, 486, L23
 Leroy, A., Bolatto, A., Stanimirovic, S., et al. 2007, *ApJ*, 658, 1027
 Levenberg, K. 1944, *Quart. Appl. Math.*, 2, 164
 Lisenfeld, U., Israel, F. P., Stil, J. M., & Sievers, A. 2002, *A&A*, 382, 860
 Liu, D., Saintonge, A., Bot, C., et al. 2024, arXiv e-prints [arXiv:2403.01202]
 Loiseau, N., Klein, U., Greybe, A., Wielebinski, R., & Haynes, R. F. 1987, *A&A*, 178, 62
 Luparello, H. E., Boero, E. F., Lares, M., Sánchez, A. G., & Lambas, D. G. 2022, *MNRAS*, 518, 5643
 Marquardt, D. W. 1963, *J. Soc. Ind. Appl. Math.*, 11, 431
 Mather, J. C., Hauser, M. G., Bennett, C. L., et al. 1990, in *Liege International Astrophysical Colloquia*, 29, Liege International Astrophysical Colloquia, ed. B. Kaldeich, 25
 McConnachie, A. W., Irwin, M. J., Ferguson, A. M. N., et al. 2005, *MNRAS*, 356, 979
 Ménard, B., Scranton, R., Fukugita, M., & Richards, G. 2010, *MNRAS*, 405, 1025
 Mennella, V., Brucato, J. R., Colangeli, L., et al. 1998, *ApJ*, 496, 1058
 Mény, C., Gromov, V., Boudet, N., et al. 2007, *A&A*, 468, 171
 Miville-Deschênes, M.-A., & Lagache, G. 2005, *ApJS*, 157, 302
 Mountfort, P. I., Jonas, J. L., de Jager, G., & Baart, E. E. 1987, *MNRAS*, 226, 917
 Muñoz, R. R., Côté, P., Santana, F. A., et al. 2018, *ApJ*, 860, 66
 Murphy, E. J., Helou, G., Condon, J. J., et al. 2010, *ApJ*, 709, L108
 Murphy, E. J., Linden, S. T., Dong, D., et al. 2018, *ApJ*, 862, 20
 Murphy, E. J., Hensley, B. S., Linden, S. T., et al. 2020, *ApJ*, 905, L23
 Neugebauer, G., Habing, H. J., van Duinen, R., et al. 1984, *ApJ*, 278, L1
 Paradis, D., Bernard, J.-Ph., & Mény, C. 2009, *A&A*, 506, 745
 Paradis, D., Veneziani, M., Noriega-Crespo, A., et al. 2010, *A&A*, 520, L8
 Paradis, D., Paladini, R., Noriega-Crespo, A., et al. 2012, *A&A*, 537, A113
 Paradis, D., Mény, C., Noriega-Crespo, A., et al. 2024, *A&A*, 691, A241
 Peel, M. W., Dickinson, C., Davies, R. D., Clements, D. L., & Beswick, R. J. 2011, *MNRAS*, 416, L99
 Planck Collaboration I. 2011, *A&A*, 536, A1
 Planck Collaboration XVII. 2011, *A&A*, 536, A17
 Planck Collaboration XVIII. 2011, *A&A*, 536, A18
 Planck Collaboration XXIV. 2011, *A&A*, 536, A24
 Planck Collaboration VII. 2014, *A&A*, 571, A6
 Planck Collaboration XI. 2014, *A&A*, 571, A11
 Planck Collaboration XII. 2014, *A&A*, 571, A2
 Planck Collaboration XIII. 2014, *A&A*, 571, A13
 Planck Collaboration XIV. 2014, *A&A*, 564, A45
 Planck Collaboration XV. 2014, *A&A*, 565, A103
 Planck Collaboration XVII. 2014, *A&A*, 566, A55
 Planck Collaboration XXIII. 2015, *A&A*, 580, A13
 Planck Collaboration XXVI. 2016, *A&A*, 594, A26
 Planck Collaboration IV. 2020, *A&A*, 641, A4
 Planck Collaboration LVII. 2020, *A&A*, 643, A42
 Planck Collaboration Int. XXV. 2015, *A&A*, 582, A28
 Planck Collaboration Int. XLVIII. 2016, *A&A*, 596, A109
 Poidevin, F., Rubiño-Martín, J. A., Dickinson, C., et al. 2018, *MNRAS*, 486, 462
 Poonj, P., Chung, A., Hoang, T., et al. 2024, *ApJ*, 963, 88
 Prandoni, I., Murgia, M., Tarchi, A., et al. 2017, *A&A*, 608, A40
 Richter, O. G., Tammann, G. A., & Huchtmeier, W. K. 1987, *A&A*, 171, 33
 Roman-Duval, J., Jenkins, E. B., Tchernyshyov, K., et al. 2022, *ApJ*, 928, 90
 Rémy-Ruyer, A., Madden, S. C., Galliano, F., et al. 2013, *A&A*, 557, A95
 Scaife, A. M. M., Nikolic, B., Green, D. A., et al. 2010, *MNRAS*, 406, L45
 Shain, C. A. 1959, *IAU Symp.*, 9, 328
 Shetty, R., Kauffmann, J., Schnee, S., Goodman, A. A., & Ercolano, B. 2009, *ApJ*, 696, 2234
 Siebenmorgen, R. 2023, *A&A*, 670, A115
 Smith, B. J., Price, S. D., & Baker, R. I. 2004, *ApJS*, 154, 673
 Smith, M. W. L., Eales, S. A., Gomez, H. L., et al. 2012, *ApJ*, 756, 40
 Smith, M. W. L., Eales, S. A., Williams, T. G., et al. 2021, *ApJS*, 257, 52
 Springob, C. M., Haynes, M. P., Giovanelli, R., & Kent, B. R. 2005, *ApJS*, 160, 149
 Tabatabaei, F. S., Krause, M., & Beck, R. 2007, *A&A*, 472, 785
 Tabatabaei, F. S., Berkhuijsen, E. M., Frick, P., Beck, R., & Schinnerer, E. 2013a, *A&A*, 557, A129
 Tabatabaei, F. S., Schinnerer, E., Murphy, E. J., et al. 2013b, *A&A*, 552, A19
 Tibbs, C. T., Watson, R. A., Dickinson, C., et al. 2010, *MNRAS*, 402, 1969
 Tibbs, C. T., Flagey, N., Paladini, R., et al. 2011, *MNRAS*, 418, 1889
 Tibbs, C. T., Paladini, R., & Dickinson, C. 2012, *Adv. Astron.*, 2012, 124931
 Tibbs, C. T., Paladini, R., Dickinson, C., et al. 2013, *ApJ*, 770, 122
 Tibbs, C. T., Israel, F. P., Laureijs, R. J., et al. 2018, *MNRAS*, 477, 4968
 Watson, R. A., Rebolo, R., Rubiño-Martín, J. A., et al. 2005, *ApJ*, 624, L89
 Weingartner, J. C., & Draine, B. T. 2001, *ApJ*, 548, 296
 Williams, P. K. G., & Bower, G. C. 2010, *ApJ*, 710, 1462
 Ye, T., & Turtle, A. J. 1991, *MNRAS*, 249, 693
 Ysard, N., Juvela, M., Demyk, K., et al. 2012, *A&A*, 542, A21
 Ysard, N., Köhler, M., Jones, A., et al. 2015, *A&A*, 577, A110
 Ysard, N., Miville-Deschênes, M. A., Verstraete, L., & Jones, A. P. 2022, *A&A*, 663, A65
 Ysard, N., Jones, A. P., Guillet, V., et al. 2024, *A&A*, 684, A34

Appendix A: Radio data

Table A.1: Radio data of LMC.

References		
Wavelength (cm)	Frequency (GHz)	F_ν (Jy)
Klein et al. (1989)		
13.03	2.30	404 ± 30
21.41	1.40	529 ± 30
73.47	0.40	925 ± 30
189.74 ¹²	0.15	1736 ± 490
Haynes et al. (1991)		
3.5	8.55	270 ± 35
6.31	4.75	363 ± 30

Table A.2: Radio data of SMC.

References		
Wavelength (cm)	Frequency (GHz)	F_ν (Jy)
Haynes et al. (1991)		
3.5	8.55	15 ± 4
6.31	4.75	19 ± 4
12.23	2.45	26 ± 3
74.94 ¹³	0.40	133 ± 10
Mountfort et al. (1987)		
13.03	2.30	31 ± 6
Loiseau et al. (1987)		
21.41 ¹⁴	1.4	42 ± 6
Ye & Turtle (1991)		
35.68	0.84	75 ± 8
Klein et al. (1989)		
374.74 ¹⁵	0.08	460 ± 200
Alvarez et al. (1989)		
749.48	0.04	415 ± 80
Shain (1959)		
1498.96	0.02	5270 ± 1054

Table A.3: Radio data of M31 ([Harper et al. 2023](#)).

Wavelength (cm)	Frequency (GHz)	F_ν (Jy)
2.5	12.0	2.73 ± 0.16
6.3	4.76	4.06 ± 0.14
21.1	1.42	8.50 ± 0.70
73.5	0.41	17.50 ± 1.90

Table A.4: Radio data of M33.

References		
Wavelength (cm)	Frequency (GHz)	F_ν (Jy)
Buczilowski (1988)		
2.8	10.70	0.48 ± 0.15
6.3	4.75	11.0 ± 0.167
11	2.70	1.68 ± 0.168
17.4	1.72	2.71 ± 0.254
21.1	1.42	2.99 ± 0.44
35.6	0.84	5.37 ± 1.22
Tabatabaei et al. (2007)		
3.6	8.35	0.78 ± 0.06
6.2	4.85	1.30 ± 0.13
21	1.42	2.76 ± 0.06

Table A.5: Radio data of NGC 253 ([Williams & Bower 2010](#)).

Wavelength (cm)	Frequency (GHz)	F_ν (Jy)
5.0	6.0	1.95 ± 0.08
6.51	4.6	2.51 ± 0.08
14.28	2.1	4.21 ± 0.12
27.25	1.1	6.90 ± 0.08

Table A.6: Radio data of NGC 4945 ([Williams & Bower 2010](#)).

Wavelength (cm)	Frequency (GHz)	F_ν (Jy)
3.57	8.4	1.69 ± 0.5
6.18	4.85	2.95 ± 0.45
11.1	2.7	5.0 ± 1.5
21.26	1.41	6.6 ± 1.98
35.6	0.84	8.3 ± 2.24

Appendix B: Local estimate of the cirrus foreground

Around each galaxy we study, we used the region outside the galaxy as defined in Section 3.3 to compare the global IR-mm emission and gas templates. We performed a linear fit to the correlations obtained on independent pixels between the observed emission in each band and the gas column density. We did this on the maps at 1° resolution with the CMB fluctuations, CIB and resolved sources subtracted.

Since foreground cirrus at high Galactic latitude is dominated by diffuse neutral gas ([Boulanger & Perault 1988](#); [Boulanger et al. 1996](#); [Planck Collaboration XVII 2014](#)), we used the HI 4-PI HI column density maps. We fit the observed dust-HI correlation as observed in each band, in independent pixels, in the surroundings of each galaxy. The average IR-HI emissivity ratios from [Planck Collaboration XVII \(2014\)](#) are used as initial guess for the fit.

Dust emission is associated to all gas phases and the contribution of dust associated to molecular or ionized gas can sometimes be significant, even at high Galactic latitude (e.g., [Lagache et al. 1999](#); [Cheng et al. 2025](#)). We therefore checked whether adding the ionized gas using [Finkbeiner \(2003\)](#) H α map and the CO gas using the [Planck Collaboration XIII \(2014\)](#) maps as additional gas tracers would improve the foreground removal.

We considered the dust-HI, dust-H α and dust-CO relationships as 3D or 4D dust-gas correlation fits. In the surroundings of the galaxies we study, we found that the contributions of the dust correlations with H α and CO were non significant. Since our goal is to subtract the emission foreground in front of the galaxies we study, we therefore restricted ourselves to the use of the dust-HI correlations around each galaxy.

The correlation between dust emission and HI column densities is fit as a linear relationship outside each galaxy, in each band from 97 μ m to 13 mm

$$I_\nu = \sigma_{\text{HI}} \times N_{\text{HI}} + y_0, \quad (\text{B.1})$$

where: I_ν is the intensity map at frequency ν , N_{HI} the HI column density in units of 10^{20} H/cm 2 , σ_{HI} represents the dust emissivity per unit HI column density and y_0 accounts for any residual background offset in the emission. We determined the best-fit values using a linear least-squares regression technique.

The dust emissivities per HI column that we obtained in each band are plotted as a function of the observed wavelength in Figure B.1 for each region around the studied galaxies separately. We observe that the Milky Way dust SEDs that we deduce are globally consistent across the whole wavelength range with what was observed on average at high Galactic latitude by Planck Collaboration XXIV (2011). Yet, we also observe differences between regions which justify our use of the locally estimated ratios rather than the average high-latitude sky values. We apply these local emissivity coefficients to the HI4PI N_{HI} maps to create templates of the Milky Way foreground emission. Towards the line-of-sight of M31, part of the HI in the disk of M31 has velocities that intercept our velocity range $[-90, 90]$ km/s and we want to avoid subtracting these as Milky Way dust. This is the only case where we observe this and hence we decided to mask this very specific region and to interpolate the HI maps in the direction of M31. Using our obtained dust emission templates for the Milky Way foreground, we subtracted these maps at all wavelengths to our convolved and (CIB+sources+ δ_{CMB}) subtracted maps for each galaxy of our sample.

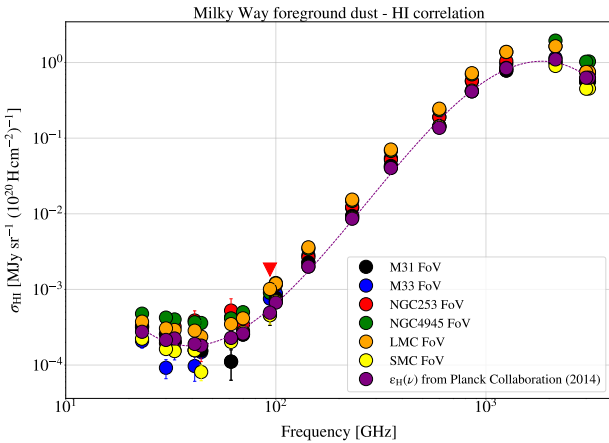


Fig. B.1: SEDs of the Milky Way foreground estimated from local dust- N_{HI} correlations around our six studied galaxies. These SEDs laws are compared to the average high-latitude values (Planck Collaboration XVII 2014). Non-detections are represented by upside-down triangles.

Appendix C: Best-fit parameters with and without AME component

Table C.1: Best-fit parameters obtained for each galaxy, using an all-components model and the model where the AME component is excluded.

Parameters	All components model						No AME model					
	LMC	SMC	M31	M33	NGC 253	NGC 4945	LMC	SMC	M31	M33	NGC 253	NGC 4945
β	1.29 \pm 0.18	0.86 \pm 0.27	1.52 \pm 0.15	0.98 \pm 0.37	1.61 \pm 0.34	1.37 \pm 0.72	1.28 \pm 0.18	0.84 \pm 0.28	1.59 \pm 0.14	1.12 \pm 0.37	1.68 \pm 0.31	1.49 \pm 0.72
$\log_{10}(\tau_{353})$	-5.19 \pm 0.05	-5.70 \pm 0.08	-5.50 \pm 0.04	-6.15 \pm 0.10	-6.54 \pm 0.07	-6.33 \pm 0.23	-5.19 \pm 0.06	-5.69 \pm 0.08	-5.50 \pm 0.04	-6.14 \pm 0.10	-6.53 \pm 0.06	-6.35 \pm 0.24
T_d (K)	24.4 \pm 2.33	27.3 \pm 4.34	18.5 \pm 1.17	24.2 \pm 4.69	24.9 \pm 3.97	24.7 \pm 7.41	24.4 \pm 2.31	27.6 \pm 4.74	18.1 \pm 1.07	22.9 \pm 4.21	24.1 \pm 3.38	23.9 \pm 6.94
EM (pc cm $^{-6}$)	27.9 \pm 23.0	23.02 \pm 6.98	4.75 \pm 3.06	1.81 \pm 1.38	2.78 \pm 2.12	5.31 \pm 3.36	34.3 \pm 24.9	30.1 \pm 3.63	7.08 \pm 2.59	3.34 \pm 1.55	4.84 \pm 1.99	6.21 \pm 3.22
C_{syn}	563 \pm 471	43.2 \pm 6.72	9.18 \pm 0.83	3.45 \pm 0.17	6.93 \pm 0.34	7.21 \pm 1.53	555 \pm 51.0	37.3 \pm 4.66	8.61 \pm 0.71	3.29 \pm 0.19	6.59 \pm 0.32	7.00 \pm 1.54
α_{syn}	-0.49 \pm 0.04	-1.14 \pm 0.14	-0.67 \pm 0.07	-0.91 \pm 0.16	-0.81 \pm 0.07	-0.81 \pm 0.18	-0.49 \pm 0.05	-1.27 \pm 0.13	-0.70 \pm 0.07	-1.06 \pm 0.25	-0.89 \pm 0.08	-0.79 \pm 0.19
δ_{CMB} (μ K)	64.7 \pm 11.7	25.8 \pm 10.4	19.9 \pm 2.91	5.07 \pm 4.06	5.15 \pm 1.25	-34.74 \pm 4.54	62.5 \pm 11.6	22.2 \pm 10.2	21.4 \pm 2.46	6.63 \pm 3.29	5.21 \pm 1.20	-33.58 \pm 4.01
C_{AME}	0.20 \pm 0.21	0.34 \pm 0.25	0.13 \pm 0.08	0.11 \pm 0.08	0.12 \pm 0.08	0.23 \pm 0.18	-	-	-	-	-	-
χ^2	8.85	4.97	1.55	8.55	4.52	2.90	7.13	5.02	2.28	6.56	5.63	1.68
χ^2_r	0.80	0.38	0.16	0.57	0.45	0.6	0.59	0.36	0.21	0.44	0.51	0.14
ϵ_{AME} (μ K/(MJy/st))	0.91 \pm 0.97	5.96 \pm 4.96	4.50 \pm 2.94	9.00 \pm 7.16	5.88 \pm 3.98	10.47 \pm 10.00	-	-	-	-	-	-
ϵ_{AME} (K/ τ_{353})	3.85 \pm 0.64	13.72 \pm 3.47	5.94 \pm 0.69	34.13 \pm 10.70	86.67 \pm 20.28	53.13 \pm 33.20	-	-	-	-	-	-

Notes. The all-components model consists of thermal dust, free-free, synchrotron, and AME emission for the galaxy as well as CMB temperature fluctuations in the background. For this model, the AME emissivities deduced from the AME best fit parameter, both normalized by the 3000 GHz flux density and by the dust optical depth τ_{353} , are also added.

Appendix D: Test on limitation of the radio data

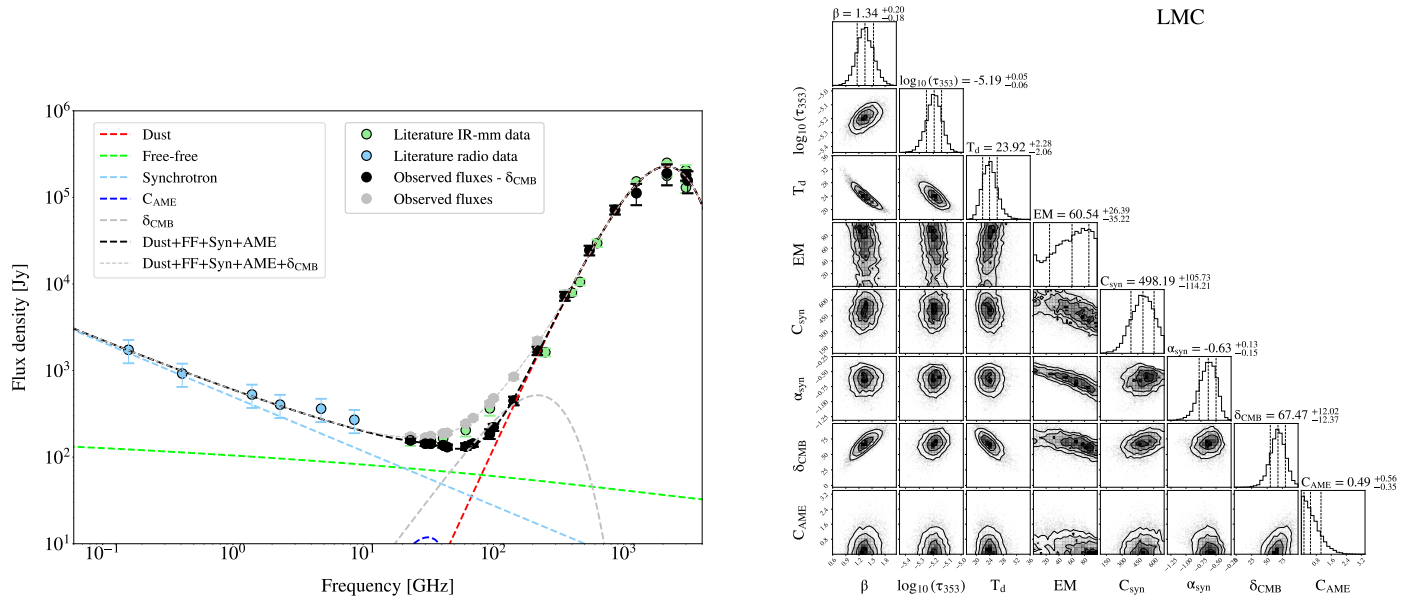


Fig. D.1: SED of LMC as observed with gray points and without CMB with black points (subtracted from the best model), and radio data in light blue (from Tables A.1) with 30% increased uncertainties. Data points from the literature (Israel et al. 2010; Planck Collaboration XVII 2011) are overlaid in green. The best fit model spectra are overlaid for the global model and individual emission components. On the right, the corner plot displays probability distributions of each model parameter, with the MCMC best-fit values indicated above each histogram.